Comprehensive FR1(C) and FR3 Lower and Upper Mid-Band Propagation and Material Penetration Loss Measurements and Channel Models in Indoor Environment for 5G and 6G

DIPANKAR SHAKYA[1] (Graduate Student Member, IEEE),
MINGJUN YING[1] (Graduate Student Member, IEEE), THEODORE S. RAPPAPORT[1] (Fellow, IEEE),
HITESH PODDAR[2] (Member, IEEE), PEIJIE MA[1], YANBO WANG[1], AND IDRIS AL-WAZANI[1]

(Invited Paper)

[1]NYU WIRELESS, New York University Tandon School of Engineering, Brooklyn, NY 11201, USA

[2]Sharp Laboratories of America, Vancouver, WA 98607, USA

CORRESPONDING AUTHOR: T. S. RAPPAPORT (e-mail: tsr@nyu.edu)

ABSTRACT Wide bandwidth requirements for multi-Gbps communications have prompted the global telecommunications industry to consider new mid-band spectrum allocations in the 4–8 GHz FR1(C) and 7–24 GHz FR3 bands, above the crowded bands below 6 GHz. Allocations in the lower and upper mid-band aim to balance coverage and capacity, but there is limited knowledge about the radio propagation characteristics in the 4–24 GHz frequency bands. Here we present the world's first comprehensive indoor propagation measurement and channel modeling study at 6.75 GHz and 16.95 GHz in mid-band spectrum conducted at the NYU WIRELESS Research Center spanning distances from 11–97 m using 31 dBm EIRP transmit power with 15 and 20 dBi gain rotatable horn antennas at 6.75 GHz and 16.95 GHz, respectively. Analysis of the omnidirectional and directional propagation path loss using the close-in free space model with 1 m reference distance reveals a familiar waveguiding effect in indoor environments for line-of-sight (LOS). Compared to mmWave frequencies, the omnidirectional LOS and non-LOS (NLOS) path loss exponents (PLE) are similar, when using a close-in 1 m free space path loss reference distance model. Observations of the omnidirectional and directional RMS delay spread (DS) at FR1(C) and FR3 as compared to mmWave and sub-THz frequencies indicate decreasing RMS DS as the carrier frequency is increased. The RMS angular spreads (AS) at 6.75 GHz are found to be wider compared to 16.95 GHz, showing greater number of multipath components from a broader set of directions in the azimuthal spatial plane when compared to higher frequencies. This work also presents results from extensive material penetration loss measurements at 6.75 GHz and 16.95 GHz using co and cross polarized antenna configurations for ten common construction materials found inside buildings and on building perimeters, including concrete walls, low-emissivity glass, wood, doors, drywall, and whiteboard. Our findings show penetration loss increases with frequency for all of the ten materials and partitions tested, and suggest further investigation of 3GPP material penetration loss models for at least infrared reflective (IRR) glass and concrete may be necessary. The empirical data and resulting models for radio propagation and penetration loss presented in this paper provide critical information for future 5G and 6G wireless communications.

INDEX TERMS 3GPP, 5G, 6G, angular spread, CI path loss, delay spread, FR3, FR1(C), InH, indoor, materials, partition loss, radio propagation, path loss, penetration loss, upper mid-band, mid-band, lower mid-band, upper 6 GHz, XPD.

I. INTRODUCTION

THE DESIRE for wide bandwidths to achieve gigabits-per-second data throughput for future sixth generation (6G) mobile phones has prompted the industry to augment the 5G spectrum allocations of mmWave Frequency Range 2 (FR2) with new spectrum above the crowded sub-6 GHz bands. Conventionally, frequencies below 6 GHz have been defined as Frequency Range 1 (FR1) by the 3GPP global mobile communications standard body [1], while the IEEE defines frequencies between 4–8 GHz as the C band. In this paper, the frequency range between 4 to 8 GHz is denoted as the FR1(C) band [1], [2], [3] (see Table 1 for the meaning of FR1(C) as well as other abbreviations in this paper). Within the past year, there has been strong international interest in the FR1(C) lower mid-band and FR3 upper mid-band spectrum for 5G and 6G mobile communications. Often heralded as the "golden band" due to the promising balance between expansive coverage and high capacity (due to wider channel bandwidth allocations than at sub-6 GHz), the 4–8 GHz FR1(C) and 7–24 GHz FR3 upper mid-band spectrum are anticipated to play a crucial role in the deployment of next-generation 5G and 6G cellular systems [4]. Agencies such as the International Telecommunications Union (ITU), the U.S. National Telecommunications and Information Administration (NTIA) and Federal Communication Commission (FCC) are considering the FR1(C) and FR3 bands for mobile operators to use alongside current incumbents such as satellite communications, earth exploration, and radio astronomy. Particularly, ITU and NTIA in the United States have put specific focus on the 7.125-8.4 GHz band, and other segments including the 4.40-4.80 GHz and 14.8-15.35 GHz, as identified by the ITU World Radio Conference 2023 (WRC-23) in Figure 1 [5]. Furthermore, the commercial significance of this spectrum is acknowledged by industry leaders, such as Nokia [6], Huawei [7], and the Alliance for Telecommunications Industry Solutions (ATIS), who have identified FR1(C) and FR3 mid-band spectrum as being crucial for future network developments. The 3rd Generation Partnership Project (3GPP) and FCC's interest in the FR3 frequencies underscore the escalating data requirements and the certain adoption of frequencies between 6-24 GHz for future global mobile usage [8]. Presently, there is limited knowledge regarding the radio propagation characteristics at these frequencies for cellular deployments. There is much exploration needed in diverse environments including indoor, outdoor, and factories. Knowing propagation behavior inside buildings is extremely critical since people spend 87% of their time indoors, as found by the National Human Activity Pattern Survey [9]. Cellphone coverage inside buildings, or penetration into buildings from outdoor cellsites, requires that radio signals interact with several building materials and partitions [10]. It is well known at frequencies below 6 GHz as well as at mmWave frequencies that narrow band and wideband (individual multipath component) fading inside buildings is generally Ricean [11], [12], [13]. In such Ricean fading environments, the presence of humans causes reflection

of multipath components (MPCs), with the additional benefit of diffraction propagation around human bodies at frequencies below 6 GHz, but there are deep body losses (tens of dB at mmWave), typically modeled with double knife-edge diffraction models [14], [15]. Penetration through various common building materials and partitions remain under-explored in the FR1(C) and FR3 spectrum as compared to other frequencies used in 1G through 5G, although some work exists in the literature as demonstrated in Section IX at the back of this paper, and for example in [10], [16], [17], [18], [19], [20], [21], [22], [23], [24], [25], [26].

There are a few empirical indoor path loss and delay spread measurements reported in the literature in the FR1(C) and FR3 spectrum. Table 2 lists the path loss exponents (PLE), RMS DS, and omnidirectional RMS AS-for-arrival (RMS ASA) reported in the literature of indoor channel measurements in FR1(C) and FR3 frequency bands. Referring to Table 2, propagation measurements in [27] conducted along an office corridor at 11 and 14 GHz using a vector network analyzer (VNA)-based channel sounding system with biconical antennas observed PLE of 1.52 and 1.59 in LOS and 3.06 and 2.76 in NLOS, using a close-in (CI) 1 m free-space reference distance [28]. Mean RMS delay spreads were reported as 19.5 ns and 17.9 ns in LOS at 11 GHz and 14 GHz, and 23.43 ns and 22.03 ns at 11 GHz and 14 GHz, respectively. Wei et al. conducted propagation measurements in university corridors in [29] with a MIMO array at 6 GHz with 100 MHz bandwidth using a sliding correlation channel sounder and recorded ∼21 ns RMS DS in LOS and ∼39 ns in NLOS. Continuous wave measurements performed along a university hallway in [30] using a signal generator and signal analyzer at 14 and 22 GHz using horn antennas with 19.5 and 22 dBi gain at the respective frequencies yielded a directional LOS PLE of 1.6 and 1.7, respectively, with CI 1 m reference distance. VNA-based propagation measurements in [31] conducted at 2.4, 4.75, and 11.5 GHz with 500 MHz and 1 GHz bandwidth in an indoor office/laboratory environment using biconical antennas yielded LOS PLEs of 1.86, 1.98 and 1.94 and NLOS PLEs of 3.33, 3.75, and 4.46 with a 1 m free-space reference distance at the three respective frequencies. The PLE in indoor environments is reported as 1.8 with 1 m free-space reference in LOS at 1.4 GHz and 4 GHz [32]. The PLEs are lower than the free-space PLE and suggest a frequency selective waveguiding effect indoors. Measurements in indoor offices and grocery/retail stores at 914 MHz report a PLE (1 m reference distance) of 2.76 considering all LOS and NLOS locations measured on the same floor of the building [33]. Indoor measurements in [34] measured diffraction loss at 10, 20, and 26 GHz around drywall, plastic board, and wooden corners, and found good agreement with the Knife Edge Diffraction (KED) model. Authors in [35] studied the RMS DS for outdoor-to-indoor (O2I) scenarios at 3.3, 6.5, 15, and 28 GHz and found higher delay spreads for O2I scenarios compared to outdoor measurements at similar distances, while a clear trend was

TABLE 1. List of abbreviations.

| Abbr.	Definitions		Abbr.	Definitions
3GPP	Third Generation Partnership Project		Low-e	Low Emissivity
5G	Fifth Generation		MTI	Minimum Time Void Interval
6G	Sixth Generation		Mcps	Mega-chips per second
AoA	Angle of Arrival		MIMO	Multiple Input Multiple Output
AoD	Angle of Departure		mmWave	Millimeter Wave
AS	Angular Spread		MPC	Multipath Component
ASA	Azimuth Spread of Arrival		Msps	Mega-samples per second
ASD	Azimuth Spread of Departure		MUT	Material Under Test
Az	Azimuth		NLOS	Non-Line of Sight
BW	Bandwidth		NTIA	National Telecommunications and Information Administration
CI	Close-In		O2I	Outdoor-to-Indoor
CIX	CI Reference Distance With XPD		PAS	Power Azimuth Spectrum
CW	Continuous Wave		PDP	Power Delay Profile
DS	Delay Spread		PL	Path Loss
EIRP	Effective Isotropic Radiated Power		PLE	Path Loss Exponent
El	Elevation		PN	Pseudorandom Noise
FCC	Federal Communications Commission		Pol	Polarization
FR1(C)	Frequency Range 1 C Band (4-8 GHz)		PTP	Precision Time Protocol
FR3	Frequency Range 3 upper mid-band (7-24 GHz)		RMS	Root Mean Square
FSPL	Free-Space Path Loss		RMSE	Root Mean Square Error
GHz	Gigahertz		SNR	Signal-to-Noise Ratio
GSM	Global System for Mobile Communications		SP	Subpath
H	Horizontal		SL	Spatial Lobe
HPBW	Half-Power Beam Width		Sync	Synchronization
IF	Intermediate Frequency		TC	Time Cluster
InH	Indoor Hotspot		TCSL	Time-cluster Spatial Lobe
IRR	Infrared Reflective		TX	Transmitter
ISAC	Integrated Sensing and Communication		UMi	Urban Microcell
ITU	International Telecommunication Union		UWB	Ultra-Wideband
KED	Knife Edge Diffraction		V	Vertical
LO	Local Oscillator		VNA	Vector Network Analyzer
LOS	Line of Sight		XPD	Cross Polarization Discrimination
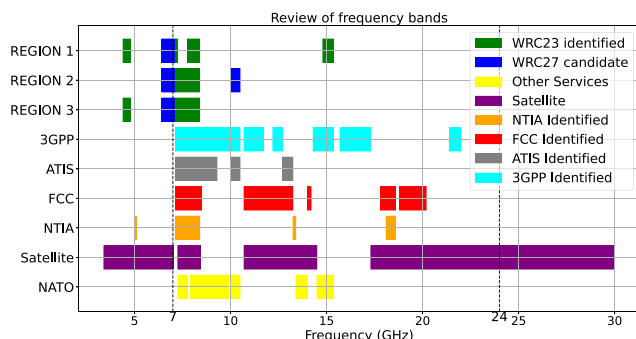
FIGURE 1. Frequency bands of interest identified across FR1(C) and FR3 by ITU, NTIA, FCC, and ATIS [5], [6], [7], [8].

not observed for the O2I delay spreads across the four frequencies.

Table 10 (see the Annex of reported penetration loss) shows an extensive literature review of relevant works for penetration into buildings and through materials in the FR1(C) and FR3 frequency bands. There have been research endeavors to characterize the penetration loss of various materials in mmWave [41], [42] and sub-6 GHz bands [16], [17]. However, investigation into the penetration loss of such materials for the FR1(C) and FR3 frequencies have been limited compared to other bands. Referring to Table 10 in the Annex, Muqaibel et al. [18] studied the propagation of ultrawideband (UWB) signals through common building materials such as drywall, plywood, wooden door, glass, brick wall, concrete block wall, styrofoam, office cloth partition and reinforced concrete wall at frequencies between 2-10 GHz. Authors in [19] measured penetration loss of wood panels 0.6, 1, and 1.4 cm thick using a narrowband swept network analyzer from 7–15 GHz and reported 1.9, 1.7, and 3.2 dB loss at 7 GHz and 2, 4.1, and 5 dB loss at 15.5 GHz. Authors in [18] measured the dielectric properties of materials (permittivity and loss tangent) to

TABLE 2. Path loss, RMS DS, and RMS ASA model parameters for indoor wireless channels in FR1 and FR3 from the literature.

S.N.	Freq. band [GHz]	Meas. BW [MHz]	Meas. System	Scenario	PLE (CI, $d_0 = 1$ m)					RMS DS				RMS ASA		Ref
					Dir (n)			Omni (n)		Dir μ [ns]		Omni μ [ns]		Omni μ [°]		
					LOS	NLOS Best	NLOS	LOS	NLOS	LOS	NLOS	LOS	NLOS	LOS	NLOS	
1	6	100	Spread spectrum sliding correlation (512 el. MIMO array)	Indoor Corridor	–	–	–	–	–	24	39	–	–	24.55	29.51	[29]
2	10.7–11.7	0.977 (1024 pts)	Swept VNA with biconical antennas	Indoor corridor	–	–	–	1.52	3.06	–	–	19.5	23.43	–	–	[27]
	14.1–15.1				–	–	–	1.59	2.76	–	–	17.9	22.03	–	–	
3	14	CW –	Signal generator and spectrum analyzer	Indoor Corridor	1.6	1.9	2	–	–	–	–	–	–	–	–	[30]
	22				1.7	1.7	1.9	–	–	–	–	–	–	–	–	
4	4.75	500	Swept VNA with biconical antennas	Indoor Office/Lab	–	–	–	1.98	3.75	–	–	12.1	15.6	–	–	[31]
	11.5	1000			–	–	–	1.94	4.46	–	–	6.8	12.1	–	–	
5	11	400	Unmodulated multitone MIMO array (2048 subcarriers)	Indoor corridor	–	–	–	1.18	3.28	–	–	Med: 10	Med: 20	–	–	[36]
6	4.5	CW	Signal generator and spectrum analyzer	Indoor Corridor	0.70	–	2.26	2.31	3.69	–	–	–	–	–	–	[37]
7	19	1000	Sliding correlation (Horn antenna)	Indoor corridor	0.6	–	–	–	–	–	–	–	–	–	–	[38]
8	4.3–7.3	15 (200 pts)	Swept VNA (Horn antenna)	Indoor office	2.06	–	2.84	–	–	–	–	–	–	–	–	[39]
9	14–17	1.87 (1604 pts)	Swept VNA (TX Horn and RX biconical antenna)	Indoor office	–	–	–	–	–	2.66		12.49		5.4		[40]
10	1.3	400	Direct RF pulse channel radar	Indoor office/factory	–	–	–	1.84	2.35	4.3	25.6	33.6	79.9	–	–	[32]
	4				–	–	–	1.84	2.44	–	–	–	–	–	–	
11	0.914	CW	Direct RF pulse channel sounder	Indoor office/stores	–	–	–	2.76		–	–	–	–	–	–	[33]
12	**6.75**	1000	Spread spectrum sliding correlation with horn antennas	Indoor office/lab	1.48	3.05	3.34	1.34	2.72	20.6	28.70	37.70	48	40.90	58.20	This Work, [2]
13	**16.95**	1000	Spread spectrum sliding correlation with horn antennas	Indoor office/lab	1.45	3.49	3.91	1.32	3.05	19.50	14.90	22.10	40.70	34.20	43.50	This Work, [2]

characterize attenuation and distortion of UWB signals when propagating through the stated materials. Landron et al. [43] measured reflection coefficients of limestone, glass, and brick wall surfaces at 1.9 GHz and 4 GHz for vertical and horizontal antenna polarizations, and found Freshnel reflection coefficient models with rough surface correction factors are adequate to model reflection. Rodriguez et al. [26] conducted measurements to study the O2I attenuation for buildings in Aalborg, Denmark using a continuous wave measurements from 800 MHz to 18 GHz, and found modern buildings presented increased penetration loss of 20-25 dB compared to old constructions. Zhang and Hwang [20] characterized the penetration loss from 0.9–18 GHz for indoor partitions such as reinforced concrete and plasterboard

walls. Measured results in [20] showed increased penetration loss with frequency for reinforced concrete wall, however, a monotonic increase with frequency was not observed for plasterboard walls. Ökvist et al. [21] presented penetration loss measurements at 15 GHz and reported losses of 24 dB for triple-pane infrared reflective (IRR) glass.

In Table 2, we have shown that many existing research on these frequency bands for Indoor Hotspot (InH) only report partial statistics for PLE, RMS DS, and RMS ASA. Our study is the first comprehensive measurement campaign to cover 6.75 GHz and 16.95 GHz in detail. Results shown later in the paper in Table 7, indicate richer multipath channels at FR1(C) and FR3 frequencies with greater temporal and spatial diversity compared to higher mmWave and sub-THz frequencies. The rich multipath propagation environment allows the implementation of higher degrees of spatial multiplexing and antenna combining for link enhancement [44]. Further, penetration losses of several materials are observed to be lower than at FR2 frequencies, as shown in Table 8 and Figure 16, suggesting less susceptibility to blockage and hence a wider coverage. We emphasize that these new bands are not well understood for cellular applications worldwide and are newly utilized by IEEE Wi-Fi 7 (6 GHz, 5.925 to 7.125 GHz) in the USA, Europe, the U.K., and Australia [45]. The wideband channel models provided are vital for 6G 3GPP standards, future Wi-Fi, and Integrated Sensing and Communication (ISAC) applications [46]. Understanding these frequency bands will not only improve network performance, enabling higher data rates, but also support advanced applications like real-time sensing and more accurate indoor localization.

This paper presents the world's first comprehensive radio propagation study for the Indoor Hotspot (InH) scenario conducted at 6.75 GHz in FR1(C) and 16.95 GHz in the FR3 frequency band using a 1 GHz bandwidth channel sounder at the NYU WIRELESS Research Center in the 370 Jay Street building, NYU Tandon School of Engineering in Brooklyn, NY. The results encompass 20 TX-RX (or T-R) locations measured at 6.75 GHz and 16.95 GHz covering distances from 11 to 97 m, along with penetration loss measurements carried out for several indoor materials, partitions, and O2I walls. The propagation analysis presented in this paper are derived from over 30,000 power delay profiles (PDP) collected across the two measurement campaigns at 6.75 GHz and 16.95 GHz at 31 dBm EIRP transmit power employing 15 and 20 dBi gain rotatable horn antennas at 6.75 GHz and 16.95 GHz, respectively, in both co-polarized and cross-polarized antenna configurations. Our previous measurement campaigns often lacked direct comparisons to industry standard models, as models at the mmWave and sub-THz frequencies were often not yet developed at the time of our work. Direct comparisons with 3GPP models are given in this paper, and offer valuable insights into the accuracy of industry-standard models and how they might need to be revised for greater accuracy and broader applicability. The key contributions in this paper are as listed:

- The NYU wideband channel sounder with new specialized dual-band co-located RF front-ends for operation at 6.75 GHz and 16.95 GHz, developed by Mini-Circuits, is described in Section II.
- The detailed calibration procedure for accurately capturing power, delay, and spatial information of multipath components is explained in Section III. Additionally, a patent-pending precision time protocol (PTP) synchronization (sync.) method implemented on the channel sounder to capture the absolute propagation delay of multipath, which has also accelerated the processing of captured PDPs is highlighted in Section III.
- Detailed measurement methodology to capture the radio propagation behavior in the InH environment, and to conduct penetration measurements for the materials and partitions is described in Section IV along with maps and material descriptions.
- Section V presents the directional and omnidirectional path loss analysis and resulting channel models for InH generated at 6.75 GHz and 16.95 GHz using the close-in 1 m free space reference distance model. The results are compared with past measurements at sub-6 GHz, mmWave, and sub-THz frequencies and 3GPP models.
- The results of penetration loss for ten construction materials and partitions at 6.75 GHz and 16.95 GHz for all four combinations of the vertical and horizontal antenna polarizations is presented in Section VII. Comparisons are made with 3GPP standard models for material penetration and past results at sub-6 GHz, mmWave, and sub-THz frequencies.
- Spatio-temporal statistics, including RMS DS and RMS ASA, extracted from the radio channel measurements at 6.75 and 16.95 GHz are presented in Section VI and compared with past measurements and 3GPP models at sub-6 GHz, mmWave, and sub-THz frequencies.

The paper organization follows the structure illustrated in Figure 2. Section II describes the channel measurement system. The calibration procedures for the channel sounding system are detailed in Section III. Section IV provides the measurement procedures employed for propagation measurements at the InH locations. Methods used for measuring material penetration loss and partition losses are also described within Section IV. The results obtained for path loss are presented in Section V. The RMS DS and ASA resulting from the multipath statistics measured are highlighted in Section VI. Observations of penetration loss for ten indoor construction materials and partitions are discussed in Section VII. Conclusions are then presented in Section VIII followed by an Annex that tabulates, in detail, the recorded penetration loss for various materials at FR1(C) and FR3 frequencies from the literature.

II. WIDEBAND FR3/FR1(C) SLIDING CORRELATION CHANNEL SOUNDER AT NYU WIRELESS

A time-domain channel sounder based on sliding correlation of pseudorandom noise (PN) sequences was
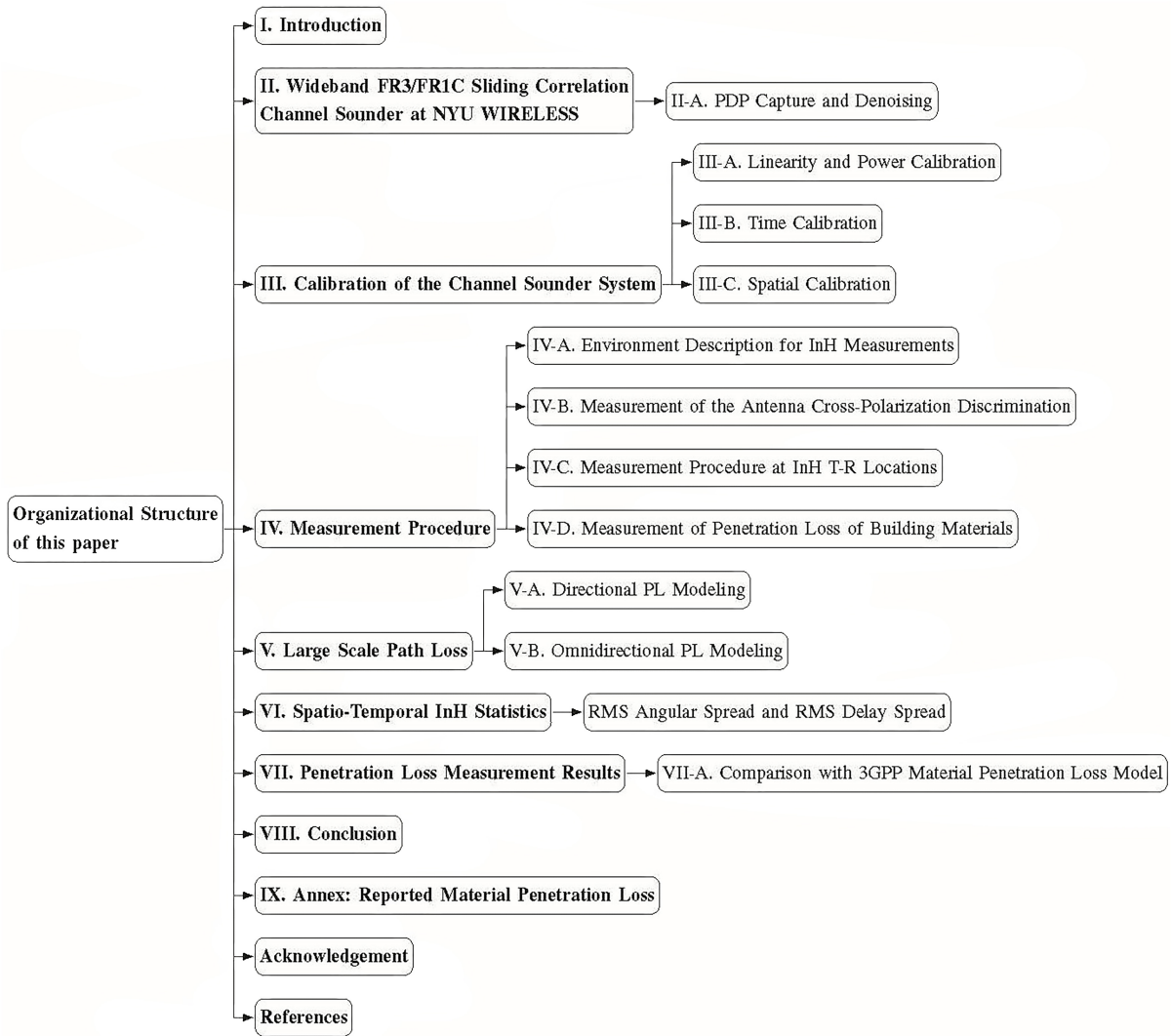
FIGURE 2. The organizational structure of this paper.

employed for wideband channel propagation and penetration measurements. The working principle of the sliding-correlation channel sounder using a PN sequence is detailed in [47], [48], and [49, Ch. 4]. As presented in Figure 3, the 500 Mcps baseband PN sequence phase modulates a 6.75 GHz carrier to result in a 1 GHz RF bandwidth (BW) signal that is connected to one of two co-located front-end modules custom developed by Mini-circuits. The module on top in Figure 3 operates at 6.75 GHz FR1(C) and the one on bottom at 16.95 GHz FR3, both with a 1 GHz bandwidth. The distinctive co-located configuration allows a simple transition between the 6.75 GHz and 16.95 GHz operating frequency bands by changing a single cable. During the operation of one module, the antenna on the other module is detached and a waveguide cover is used on the flange. Additionally, RF absorbent foam is used to cover the front surface of the unused module to avoid unwanted multipath due to the stacked design.

The FR1(C) module operating at 6.75 GHz directly transmits the broadband signal through a 15 dBi gain and a 30-degree half-power beamwidth (HPBW) horn antenna, achieving an effective isotropic radiated power (EIRP) of 31 dBm to stay within licensed emission power level of 35 dBm. As was reported in [50], the mmWave spectrum is more than four orders of magnitude below ionizing radiation, and thus FR1(C) and FR3 frequencies are more than five orders of magnitude below the ionizing frequency range. It was shown that nothing has been found other than RF heating that can cause abnormal cell growth [51]. Likewise, the front-end module designed for 16.95 GHz operation employs a heterodyne approach to upconvert the 6.75 GHz intermediate frequency (IF) signal to a RF signal at 16.95 GHz with 1 GHz bandwidth and transmits using a 20 dBi horn antenna and 31 dBm EIRP. The FR3 TX and RX front-end modules use a 7.9 GHz local oscillator (LO) signal, fed into a tripler, yielding a 23.7 GHz output that is subsequently fed
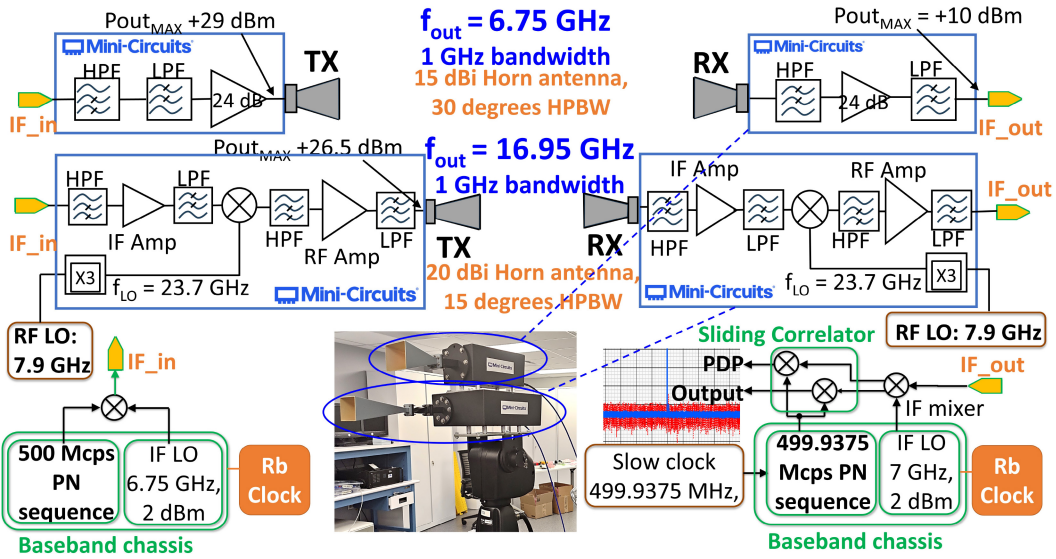
FIGURE 3. The FR1(C) and FR3 channel sounder system with co-located dual-band RF front-end modules developed by Mini-Circuits. The module on top operates at 6.75 GHz and the bottom module at 16.95 GHz.
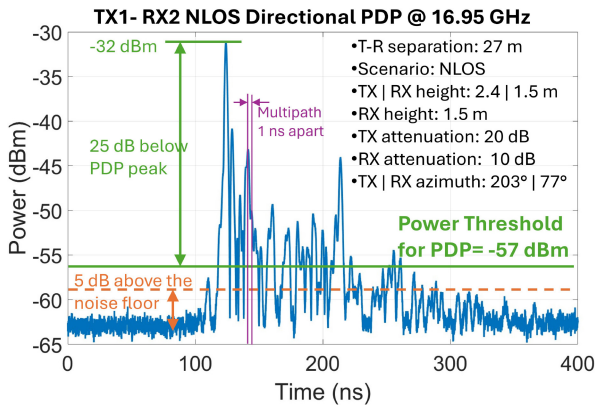

FIGURE 4. A typical directional PDP collected during measurements using the channel sounder with rotatable horn antennas. The power amplitude threshold applied to the PDP is the higher among 5 dB above the noise floor or 25 dB below PDP peak. Here, 25 dB below PDP peak is selected.

into a high-side injection mixer that produces a 16.95 GHz signal.

At the receiver, the signal, once down-converted, is passed through a sliding correlator with a 499.9375 Mcps PN sequence that results in a time-dilated PDP. The TX and RX front-end modules are mounted on mechanically rotatable gimbals with 1° spatial resolution that have a 360° range of motion in the azimuth and 120° in elevation. The wide bandwidth of 1 GHz allows the channel sounder to overcome frequency selectivity that narrowband and swept narrowband systems are prone to and resolve close multipath in temporal domain (up to 1 ns apart, example in Figure 4) to ensure accurate location and penetration measurements. The polarization of the horn antennas are changeable between vertical (V) and horizontal (H) polarization using waveguide twists at both bands. During InH location measurements, V-V co-polarized or V-H cross-polarized antenna configuration is

used. Moreover, a total of four antenna configurations V-V or H-H co-polarized, and V-H or H-V cross-polarized are used for measurement of each material under test (MUT) during material and partition penetration measurements. The specifications of the channel sounding system are detailed in Table 3.

A major difference compared to previous campaigns is the implementation of a PTP-based synchronization algorithm, described in detail in Section III-B. The time sync algorithms employed are critical to ascertain the exact propagation delay of MPCs between the TX and RX with nanosecond accuracy. As the channel sounder TX and RX operate fully untethered, in past campaigns the TX and RX LOs–indicated in Figure 3–lost synchronization after a few hours of operation during a measurement day lasting over 10 hours. The loss in time sync in many propagation measurement campaigns is unpredictable and occurs unbeknownst to the operators. As a result, in the past, the PDPs captured could have abrupt shifts in absolute timing or time drift which, if ignored, would result in erroneous MPC propagation delays. To cure such synchronization issues in the past, intensive post-processing efforts were required to estimate the accurate multipath delay using site-specific information and ray tracing to realign the PDPs precisely in propagation time before any statistics could be processed [52], [53], [54], [55], [56]. The measurements described here are the first which have used the patent-pending synchronization method described in Section III-B through the use of a Wi-Fi side channel link.

A. PDP CAPTURE & DENOISING
The channel sounder captures arriving MPCs as amplitude peaks at different delays in a PDP. The sliding correlation results in a processing gain of 39 dB due to the time

TABLE 3. System parameters for the upper-mid band channel sounder at NYU WIRELESS.

Carrier Frequency	6.75 GHz	16.95 GHz
Free Space PL at 1m reference distance	49 dB	57 dB
Baseband signal	11th order PN sequence (2047 chips)	
TX PN Code Chip Rate	500 Mcps	
TX PN Code Chip Width	2.0 ns	
RX PN Code Chip Rate	499.9375 Mcps	
Slide factor	8000	
Digitizer Sampling rate at RX Oscilloscope	2.5 Msps	
RF BW (Null-to-null)	1 GHz	
Max Transmit Power (fed into the horn antenna)	29 dBm	26.5 dBm
TX/RX Antenna Type	Pyramidal Horn Antenna	
TX/RX Antenna Dim.	3.75"×2.65"	3.08"×2.33"
TX/RX Antenna Far-field	41 cm	69 cm
TX/RX Antenna Gain	15 dBi	20 dBi
TX/RX Ant. HPBW (Az/El)	30° / 30°	15° / 15°
XPD	35 dB	38 dB
Max EIRP	44 dBm	46.5 dBm
Max EIRP used	31 dBm	
Max Measurable Path Loss (at 5 dB SNR)	155.6 dB	159.2 dB
TX Polarization	Vertical/Horizontal	
RX Polarization	Vertical/Horizontal	
TX/RX Waveguide Size	WR137	WR62

FIGURE 5. Results of the channel sounder calibration for 16.95 GHz operation. The system has a linear operating range of 50 dB, which is maintained by proper attenuator settings during field measurements.

dilation that occurs as the PN sequences slide past each other (processing gain $= 10 \times \log_{10}$(slide factor), Table 3, [47]) that allows for detection of weak MPCs. The time-dilated PDP is captured at the RX oscilloscope at the digitizer sampling rate in 81880 samples corresponding to 4094 ns max propagation delay. Thus, 20 samples in a time-dilated PDP is equivalent to 1 ns of propagation delay [55], [57]. At each capture, 20 instantaneous PDPs are averaged and recorded by the system along with the angular information of the gimbal position and different operating parameters [48]. Before processing the PDPs, a power amplitude thresholding is preformed. As illustrated in Figure 4, the higher threshold between 5 dB above the noise floor (found by averaging power in the last few hundred nanoseconds of the PDP) and 25 dB below the PDP peak is selected and all powers below this threshold are discarded. The power thresholding removes any dependency of the modeling on hardware dynamic range.

III. CALIBRATION OF THE CHANNEL SOUNDER SYSTEM
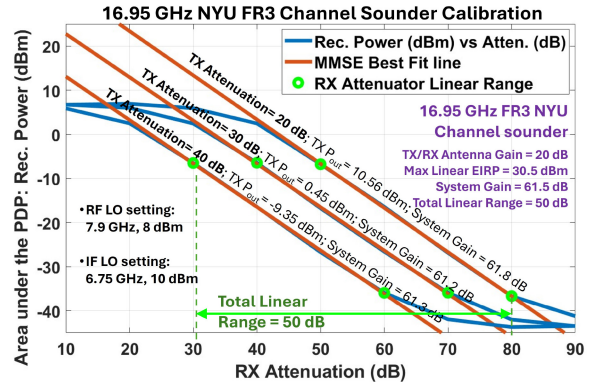The calibration for InH location measurements is an important step to ensure accurate capture of the power, delay, and direction of MPCs. Calibration is conducted at least twice a day–once at the beginning of the measurement day and once at the end–to assure daily and long-term accuracy. The NYU WIRELESS Channel sounder is calibrated in three phases:

A. LINEARITY AND POWER CALIBRATION
The linear range of operation, power limits, and system gain of the RX are defined and confirmed by measurement twice daily, once at the beginning and once at the end of each day. The transmit power applied to the TX horn antenna is measured with a Keysight N1913A power meter via the Keysight N8487A power sensor pre-calibrated to a 0 dBm reference source within the power meter. The TX attenuator and LO powers are set to keep the TX power within the limit of 35 dBm permitted by the FCC experimental license and ensure linearity of the PDPs captured during measurements. A free space PL measurement at a distance beyond 5×far-field distance (D_f) of the horn antennas helps confirm the accuracy of the received power for the transmit power used. A 4 m separation is selected with a 1.5 m TX and RX height to capture a single LOS path avoiding any reflection paths, adhering to the calibration criteria described in [58]. During calibration, power obtained by integrating the area under the curve for the first PDP peak yields the total received power in the LOS path for different configurations of the TX and RX attenuator and LO input powers [58], [59]. Figure 5 shows the calibration results of the 16.95 GHz front-end. Varying the TX and RX attenuators allows for a total 50 dB linear operation range during the penetration measurements over a 150 dB power range. Calibration at the end of the day typically shows differences of less than 0.2 dB for this FSPL calibration step.

B. TIME CALIBRATION
Accurate measurement of the absolute multipath delay during the InH location measurements requires correct implementation of time calibration, so as to assure that time drift does not cause the absolute timing to slip throughout a day of measurements. Before the measurement day, the two

separate Rubidium (Rb) clocks used each at the TX and RX are synchronized with each other overnight (12-13 hrs) using a physical cable to ensure accurate time synchronization. During system startup each day, two Raspberry-Pi computers connected to each Rb clock on the TX and RX are initiated to run a patent-pending PTP synchronization for absolute timing over a Wi-Fi link, as detailed in [55]. The Wi-Fi side channel link is operational throughout the day for continual adjustment of the frequency and phase errors between the Rb clocks to minimize time drift. Following the linearity and power calibration (explained in Section III-A) at the start of the day, the PDP which captures the single LOS peak is circular shifted by the PDP capture software at the RX, to match the free-space propagation delay of 13.3 ns for the four-meter calibration distance. Then, the TX and RX are moved to the desired location for measurements.

Upon completing measurements at a TX-RX location, the TX and RX are returned to a 4 m separation–at the location linearity and power calibration was performed–to remeasure the propagation delay for the LOS path and capture any minor drifts (typically within few nanoseconds) in the propagation delay. Without the PTP synchronization method described in [55], past measurement campaigns at NYU WIRELESS with separated Rb clocks would suffer time drift of several hundreds of nanoseconds during the 4-5 hr measurement duration at each location. The large time drifts were corrected in past campaigns with ray-tracing using NYURay [53], [57] to obtain true time-of-flight of MPCs that was augmented with the measured PDPs to correct time drift or with time drift tracking [52] that recorded the change in propagation delay of the same MPC over a few minutes and assumed the same linear rate of time drift during the several hours spent to measure each TX-RX location. The present campaign uses an active synchronization method that continuously synchronizes the Rb clocks and the PDP propagation delays against a reference MPC during the several hours of measurements at each TX-RX location, using patent-pending methods in [55]. The time calibration is repeated for every TX-RX location measured throughout the day and the minor drifts observed after measurements at a T-R location are recorded to correct the measured data in post-processing to obtain the absolute propagation delay of MPCs. The drift is found to be unaffected by the movement of TX and RX carts to respective locations [55].

C. SPATIAL CALIBRATION

At every TX-RX location, the TX and RX antennas are raised to 2.4 m and 1.5 m above the ground, respectively. Special care is required in correctly setting the heights, and horizontal and vertical leveling of antennas. The unused antenna is detached and a waveguide cover is used on the flange along with RF absorbent foam covers before the measurements to avoid undesired multipath due to the stacked design of the RF front-end modules. The geographical North is used as the spatial 0° pointing reference at each TX-RX location pair for consistent AOA/AOD recording across

all locations and spatial coordination between TX and RX during measurements.

Once the calibration process (linearity and power, time, and space) is complete, the channel sounder is ready for multipath propagation measurements at each InH TX-RX location pair. The measurement procedures are subsequently described in Section IV-C.

The calibration to conduct penetration measurements involves the completion of the linearity and power calibration, detailed in Section III-A. Particularly, the attenuator settings determined from the linearity calibration are adjusted during penetration measurements, detailed in Section IV-D, to ensure the received power falls in the linear range of operation, especially when measuring the cross-polarized antenna configurations.

IV. MEASUREMENT PROCEDURE

A. ENVIRONMENT DESCRIPTION FOR INH MEASUREMENTS

The InH measurement campaign is conducted in the NYU WIRELESS Research Center at 370 Jay Street, Brooklyn, NY. The environment is a typical open office space with cubicles, office rooms, labs, and conference rooms. The walls are mostly drywall with some labs and conference rooms having clear glass panels. The TX locations are marked as different color stars and RX locations as circles of the corresponding color on the floorplan presented in Figure 6. Identical T-R locations are measured at both frequency bands. Table 4 lists the T-R locations in LOS and NLOS for the 16.95 GHz FR3 measurements, encompassing 7 LOS and 13 NLOS T-R location pairs. The T-R separation for the locations range from 11 m to 97 m. No outages are observed at any of the T-R locations in both bands with a transmit EIRP of 31 dBm and link margin (at 5 dB SNR) of 156 dB at 6.75 GHz and 159 dB at 16.95 GHz.

B. MEASUREMENT OF THE ANTENNA CROSS-POLARIZATION DISCRIMINATION

During propagation, interaction with the environment can cause the transmitted signal energy to be captured in cross-polarized antenna orientation. Particularly, different materials can exhibit varying penetration loss for co and cross-polarized antenna configurations [58]. Thus, observing the cross-polarization discrimination (XPD) facilitates the characterization of energy captured in the orthogonal orientation. The InH location measurements, elaborated subsequently in Section IV-C, captures the MPC propagation with V-V co-polarized and V-H cross-polarized (TX in V; RX in H) horn antenna configurations. Further, the penetration measurements, detailed in Section IV-D, uses all four possible polarizations during the penetration loss measurements of each material. To accurately determine material penetration loss, the free space XPD must be measured. Figure 7 shows the antenna XPD measured for the channel sounder system at (a) 6.75 GHz and (b) 16.95 GHz in V-V and V-H polarizations, using the calibration method
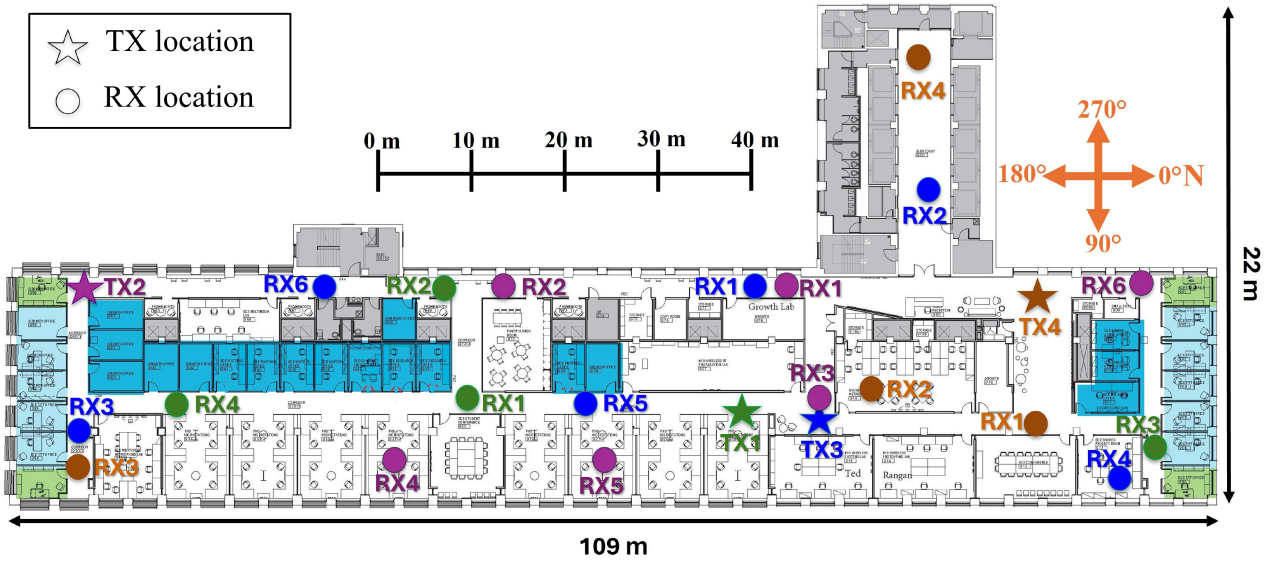
FIGURE 6. The NYU WIRELESS research Center at 370 Jay Street, Brooklyn, NY is a typical open office space with cubicles, offices, and conference rooms. The four TX locations are indicated as different color stars with corresponding RX locations as circles of the same color.

TABLE 4. TX-RX location pairs for indoor measurements at 16.95 GHz in FR3 and 6.75 GHz in FR1(C).

TX	Loc Type	RX	T-R Separation (m)
TX1	LOS	RX1	24.6
		RX4	51.0
	NLOS	RX2	27.0
		RX3	37.6
TX2	LOS	RX1	64.0
		RX2	37.2
		RX6	97.0
	NLOS	RX3	67.3
		RX4	32.2
		RX5	49.0
TX3	LOS	RX5	19.3
	NLOS	RX1	12.3
		RX2	22.3
		RX3	65.6
		RX4	30.0
		RX6	49.5
TX4	LOS	RX1	11.4
	NLOS	RX2	17.1
		RX3	87.0
		RX4	23.5

(a)

(b)

FIGURE 7. Measurement of the antenna XPD at (a) 6.75 GHz with 15 dBi, 30° HPBW WR137 horn antennas, and (b) 16.95 GHz with 20 dBi, 15° HPBW WR62 horn antennas.

in [58]. Waveguide twists at WR-137 and WR-62 facilitate the change in polarization.

To obtain empirical XPD for the horn antennas used on the FR1(C) and FR3 channel sounders, measurements of FSPL are made for the different antenna polarization configurations starting in the far field from T-R separation distances of 3 m with increments of 0.5 m up to 6 m. An open lab area is used to ensure the ground and ceiling multipath are avoided and only LOS path is captured [60]. The difference in path
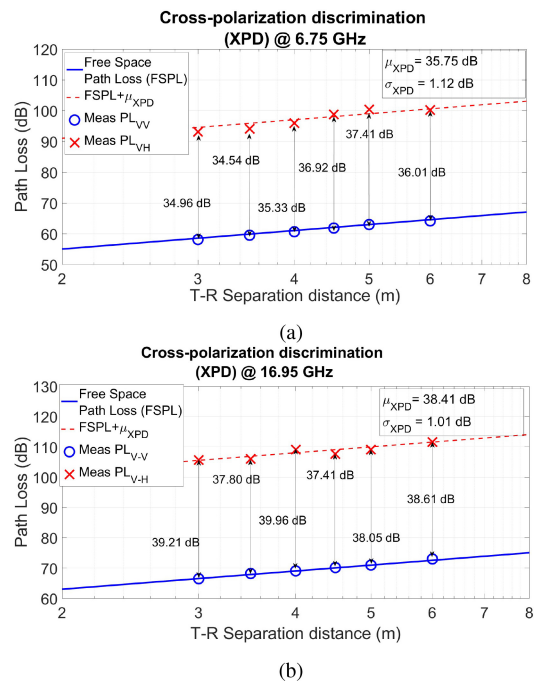
loss (PL) between the co-polarized (V-V or H-H) and cross-polarized (V-H or H-V) configurations at a T-R separation distance, d, yields the XPD, as shown in (1). A mean XPD of 35.75 dB is observed at 6.75 GHz with $\sigma_{XPD} = 1.12$ dB. Likewise, mean XPD at 16.95 GHz is obtained as 38.41 dB with $\sigma_{XPD} = 1.01$ dB.

$$XPD(d)[dB] = PL_{V-V}(d)[dB] - PL_{V-H}(d)[dB], \quad (1)$$

where,

$$PL[dB] = P_t[dBm] - P_r[dBm] + G_{TX}[dBi] + G_{RX}[dBi]$$

P_t in (1) denotes the transmit power recorded with the Keysight N1913A power meter during calibration (Section III-A). P_r represents the power in the first arriving multipath in the PDP. G_{TX} and G_{RX} are the antenna gains.

C. MEASUREMENT PROCEDURE AT INH T-R LOCATIONS

The InH multipath statistics are obtained by capturing the propagation delay, power, AOD, and AOA of all MPCs at each TX-RX location in a two-step process: rapid RX scans, followed by RX azimuthal sweeps in HPBW steps.

First, the RX completes rapid continuous azimuthal scans (rapid scan) for each TX boresight AOD to rapidly determine the TX AODs with significant energy received at the RX. To initiate the rapid scans, as taught in [52], the TX and RX are pointed at the direction with strongest received power; boresight in LOS and a strong reflection direction in NLOS. The strongest received power is ascertained by moving the TX and RX antennas in one-degree steps observing fractions of a dB change in the received power. This careful, vernier pointing approach allows us to identify the center, or exact pointing angle, for maximum power of the strongest MPC that arrives in the captured PDP. For each TX AOD, the RX performs a continuous 360° rapid scan across the azimuth plane. The TX is rotated in increments of HPBW until rapid scans are performed for each AOD. For each TX AOD the strongest peak received power is recorded within the PDP. A threshold value is established at 30 dB below the strongest received peak power across all TX AODs. Only the TX AODs with peak received power exceeding this threshold are selected for the RX azimuth sweeps. The rapid scans allow a capture of the complete AOD statistics at each TX-RX location, whereas campaigns before [52] relied on performing the RX azimuth sweeps for just the strongest few AOD selected through visual estimation or a TX azimuth sweep for the strongest RX AOA [54]. While the past approach was accurate [61], the current method is more complete and faster, as well.

Once key TX AODs are identified through rapid scan, the TX is pointed to the strongest TX AOD and the RX AOA with the strongest received power is identified. The PDP captured for this AOD-AOA pair is stored and the highest peak in the PDP is marked as the 'reference MPC' for implementing PTP synchronization [55]. After RX completes each azimuthal sweep, the TX and RX return to the AOD-AOA pair of the reference MPC and recapture the PDP to correct any drift in the propagation delay accumulated during an azimuthal sweep to implement successive drift correction [55, Algorithm I].

With key TX AODs and the reference MPC identified, the RX azimuthal sweeps, where the RX is rotated 360 ° in the azimuth in HPBW increments, are initiated to capture multipath in the channel. Five different RX azimuthal sweeps, as shown in Table 5, are completed for each TX AOD. With the TX and RX at boresight elevation, the RX steps through the azimuth in HPBW steps, referred to as Sweep#1 in Table 5. At each AOA, during the azimuthal

TABLE 5. TX/RX elevation angles for different RX azimuthal sweeps for a fixed TX azimuth angle at each TX-RX location.

Sweep#	TX elevation	RX elevation
1	TX is kept at *boresight* elevation	RX is kept at *boresight* elevation. RX is then swept 360° in the azimuth plane in HPBW steps.
2	TX is kept at *boresight* elevation	RX is *tilted down by one HPBW* (30° at 6.75 GHz/15° at 16.95 GHz). RX is then swept 360° in the azimuth plane in HPBW steps.
3	TX is kept at *boresight* elevation	RX is *tilted up by one HPBW* (30° at 6.75 GHz/15° at 16.95 GHz). RX is then swept 360° in the azimuth plane in HPBW steps.
4	TX is *tilted down by one HPBW* (30° at 6.75 GHz/15° at 16.95 GHz).	RX is kept at boresight elevation. RX is then swept 360° in the azimuth plane in HPBW steps.
5	TX is *tilted down by one HPBW* (30° at 6.75 GHz/15° at 16.95 GHz).	RX is *tilted down by HPBW* (30° at 6.75 GHz/15° at 16.95 GHz). RX is then swept 360° in the azimuth plane in HPBW steps.

scans, the RX averages 20 instantaneous PDPs and logs the system and spatial information corresponding to the captured directional PDP. In the 16.95 GHz FR3 campaign, an RX azimuthal sweep includes 24 AOAs corresponding to the 15° HPBW (15°×24 = 360°), while the 6.75 GHz FR1(C) campaign includes 12 AOAs using a 30° HPBW (30°×12 = 360°). The spatial resolution capability for the captured MPCs is determined by the resolution of the antenna pattern available for the antenna. Although the wider beamwidth may capture multiple MPCs that are not resolvable in space within the measured PDP, de-embedding methods can be applied to extract MPC angles with a degree resolution. Methods such as the antenna de-embedded multipath extraction (ADME), described in [62], are employed during post-processing for one-degree spatial resolution of MPCs.

Omnidirectional PDPs are synthesized from directional PDPs using the method described in [61] despite different antenna beamwidths to obtain omnidirectional channel statistics in Sections V and VI. Combining the directional PDPs captured during the azimuth sweep, stepping the TX/RX antenna in HPBW steps results in a flat gain profile across the azimuth plane, as detailed in [61]. The assumption is that the antenna gain is flat across the 3-dB beamwidth, which is a reasonable approximation since if an MPC arrives at an angle that falls at the edge of the RX antenna HPBW, the adjacent pointing direction shall receive additional energy, which is considered in the overall received power computation. This was rigorously proven in [61] using both field measurements and canonical antenna patterns. Similarly, the TX/RX antenna elevation is also changed based on the HPBW of the horn antenna employed. As a

result, the MPCs are captured in 3D space with a flat gain profile equaling the boresight antenna gain in magnitude, which was proven analytically and experimentally to be remarkably accurate [61].

Following Sweep#1, for the same particular TX AOD, the RX elevation is down- and up- tilted by HPBW for sequential azimuthal sweeps (Sweep#2 and Sweep#3 in Table 5). For Sweep#4, the TX elevation is downtilted by HPBW and the azimuthal sweep is performed with RX at boresight elevation. Then, Sweep#5 is conducted with both TX and RX downtilted by HPBW. The TX then moves to the next identified TX AOD and the five RX azimuthal sweeps are repeated until all identified TX AODs are measured. After the TX steps through all identified AODs, the RX azimuthal sweeps are repeated for a cross-polarized (V-H) antenna configuration, whereby the TX horn antenna is oriented in V-polarization and the RX horn antenna in H-polarization. Using the measured cross-polarization discrimination of 35.7 and 38.4 dB at 6.75 GHz and 16.95 GHz respectively (Section IV-B), only the TX AODs that exhibited a peak received power in co-polarized (V-V) configuration of 30 dB above the noise floor during rapid scans are measured. The attenuation at RX must be lowered to capture the much weaker multipath in the V-H configuration due to increased cross-polarization propagation loss [63]. This exhaustive, detailed approach requires about 4-5 hours for each T-R location pair, allowing for 2 locations to be measured per day.

After collecting directional PDPs from RX azimuthal sweeps over all key TX AODs at a T-R location pair, post processing on measured PDPs is conducted by applying a power threshold to each directional PDP. The higher received power of either 5 dB above the noise floor or 25 dB below the PDP peak is selected as the threshold and powers below it are ignored in the processing of channel statistics [57, Sec. IV-B]. The power azimuth spectrum (PAS) generated from the directional PDPs at each T-R location produced wide spatial lobes with power received at several contiguous HPBW pointing directions. A spatial lobe is defined as contiguous pointing directions with received power exceeding a spatial lobe threshold (SLT) in the PAS, below which powers in the PAS are ignored for calculating angular statistics such as RMS AS (Section VI) [57]. An SLT of 10 dB below the peak received power in the PAS (orange dotted-circle in Figure 8) is used for defining the spatial lobes in the InH campaigns. An example of a PAS recorded for different TX AOD and RX AOA in the 16.95 GHz campaign for the TX1-RX2 pair (Figure 6) is depicted in Figure 8.

D. MEASUREMENT OF PENETRATION LOSS OF BUILDING MATERIALS

The penetration loss, L, for a partition or material using both co-polarized or cross-polarized antenna configuration, is determined by observing the difference between the received powers, P_r, at identical T-R separation distances, first in free-space and then with the MUT placed halfway between the line-of-sight path from TX to RX, with a path that is
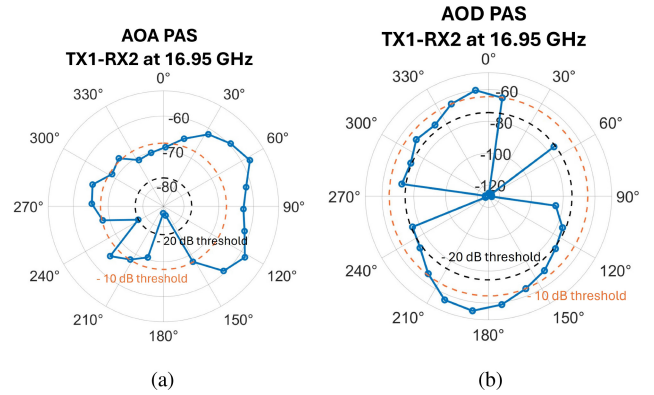

FIGURE 8. Power Azimuth Spectrum for TX1-RX2 in the 16.95 GHz campaign at: (a) RX AOAs (b) TX AODs. [T-R separation: 27 m].

perpendicular to the width of the MUT (e.g., on boresight, or on normal incidence), given by (2). P_r in (2) is obtained as the power received in the first arriving multipath in the captured PDP ignoring the other multipath [16], [59]. The 1 GHz bandwidth channel sounder allows temporal resolution of multipath up to 1 ns apart (e.g., 1 foot or 0.3 m) to ensure that reflected multipath are not within the first arriving LOS multipath component in a PDP and thus avoiding frequency selectivity of narrowband systems [60].

$$L[dB] = P_r^{FS}[dB] - P_r^{MUT}[dB], \qquad (2)$$

Measurements are made for three T-R separation distances of 2.0, 2.5, and 3.0 m (all measured distances are in the far field). Following the measurement of P_r^{FS}, the MUT (the MUT dimensions exceed $15 \times \lambda$ in all directions for each MUT) is placed halfway between the TX and RX to ensure the entire wavefront from each horn antenna illuminates the MUT. When measuring in-situ partitions, such as a drywall partition in an indoor corridor or wooden doors in rooms that prevented the TX and RX from being spaced equally, the TX is placed at a fixed separation of 1 m, while the RX is moved further at distances ranging from 1 to 2 m from the MUT to achieve the overall T-R separation distance of 2 to 3 m.

After positioning the TX and RX on either side of the MUT with a fixed separation, the TX and RX antenna orientations in both co and cross polarization are adjusted to establish a boresight configuration with the strongest first-arriving (LOS) multipath component. To mitigate potential RX antenna misalignment effects due to large HPBWs, the RX antenna is subsequently moved in azimuth and elevation by 1° increments around its boresight, resulting in a total of five PDPs recorded at each RX pointing direction. The penetration loss, L, at each distance is obtained by subtracting the linear average of these five recorded powers expressed in dB, P_r^{MUT} from P_r^{FS}, as shown in (2). Once L at each distance is calculated, the average penetration loss for the MUT is recorded as the mean of L in linear scale at the different distances. Thereafter, P_r^{MUT} and P_r^{FS} are obtained for V-H, H-V, and H-H antenna polarization. Finally, L_{VV}

FIGURE 9. Panels of different MUTs, such as drywall and wood were measured in a lab setup, whereas partitions, such as IRR glass walls required TX and RX set up on both sides of the MUT.

and L_{HH} are linearly averaged to obtain L for co-polarized antennas, and L_{VH} and L_{HV} for cross-polarized antennas.

Ten common indoor materials are measured. Panel sheets of the all the tested MUTs are employed to ensure a uniform material upon which the incident wavefront impinges. Images of the materials and partitions being measured are shown in Figure 9 and specifications are listed below:

- Drywall panel: Penetration through a USG Sheetrock brand gypsum drywall panel is measured. Dimensions of the drywall sheet are 4 ft×8 ft with 3 cm thickness.
- Birch Wood panel: A thick Birch plywood panel with 13 plies pressed together is used as the MUT for penetration measurement. The plywood panel has dimensions of 4 ft×8 ft with 2 cm thickness.
- Whiteboard: A rollable glass whiteboard with front and back writing faces is used for the penetration measurement. The whiteboard has a tempered glass finish over the laminated backing and is mounted on a metallic rollable frame. Dimensions of the whiteboard are 72"×40" with 3 cm thickness.
- Low-emissivity (low-e) or Infrared reflective (IRR) glass window: The window used for the measurement is a 59"×59" sliding panel with low-e double pane glass. Argon gas is filled in the cavity between the two panes and the window has a U-value rating of 0.29 (insulating capability of the glass, lower values indicate greater insulation [64]). Total thickness of the two panes is 2 cm. The outer frame of the window is white vinyl plastic.

Other common building partitions and walls such as plasterboard wall, cinderblock wall, and doors found in-situ within the building were also measured. An O2I penetration was measured with the massive glass curtain

wall on the perimeter of the 370 Jay Street building. The details of the in-situ indoor and O2I partitions are as follows:

- Wooden Door: Large capacity lecture halls at the NYU Tandon School of Engineering have a large wooden double door. The door is made of a fire safety rated solid wood core with 4.5 cm thickness. The door has door handles on one side and a push bar on the other side. The TX and RX heights were raised for the incident wave to impinge on a uniform door surface.
- Steel Door: Hallway entrances and some labs in the 370 Jay Street building at NYU Tandon use large doors with a skin of steel material. The steel door also has a metal push bar at the middle of the door. The TX and RX heights were raised to ensure penetration loss of a uniform steel door (without the metal push bar) was captured.
- Clear glass wall: The measured partition is a single panel transparent glass wall without any coating having 0.5 cm thickness used on the periphery of the Wireless RF Propagation Lab at 370 Jay Street.
- Low-e or IRR glass wall: The 370 Jay Street building has a glass curtain wall on the ground floor. Double-pane tinted glass with 1/2" thick panels and Argon gas filling between the glass panes is used for the curtain wall with individual panels supported by a metal frame. Additionally, the glass is tinted to reduce visibility from the outside and enhance thermal efficiency. The glass achieves a U-value of 0.26. The total thickness of the glass panels is 3 cm.
- Cinderblock wall: Some classroom partitions on the NYU campus are cinderblock walls with a coat of paint. The cinderblock wall measures 22 cm thick. Some foam soundboards are placed with irregular spacing on the concrete walls for sound absorption in the classroom.
- Plasterboard wall: The room partitions in the NYU WIRELESS Research Center are composed of sheets of drywall (or plasterboard) placed on a metal frame. Typical thickness of such partitions are 13.7 cm. Some plasterboard partitions are also known to have metal studs between the sheets. A stud detector helped ensure no studs were present in the region of the measurement.

The collection of the data from propagation measurements at the 20 InH T-R locations and penetration measurements for ten different materials and partitions is followed by post-processing using methods described in Sections V–VII to yield meaningful statistics, results and comparisons.

V. LARGE SCALE PATH LOSS
The CI 1 m free space reference distance model (3), for describing the path loss is employed on the directional and omnidirectional path loss measurements. The CI model efficiently describes PL with a single PLE (n) with

TABLE 6. Directional and omnidirectional CI PL model parameters for 6.75 and 16.95 GHz FR1(C) and FR3 InH campaigns, with comparison at 28, 73 and 142 GHz FR2 campaigns, and 3GPP models [66].

Campaign	Distance (m)	Antenna HPBW (TX/RX)	Directional path loss						Omni path loss			
			LOS		NLOS Best		NLOS		LOS		NLOS	
			n	σ (dB)	n	σ (dB)	n	σ (dB)	n	σ (dB)	n	σ (dB)
6.75 GHz (This work)	11-97	(30°/30°)	1.48	3.01	3.05	9.23	3.34	13.09	1.34	3.51	2.72	9.21
6.75 GHz (3GPP)	1–150	–	–	–	–	–	–	–	1.73	3	3.19	8.29
16.95 GHz (This work)	11-97	(15°/15°)	1.45	1.87	3.49	8.23	3.91	14.36	1.32	2.66	3.05	8.11
16.95 GHz (3GPP)	1–150	–	–	–	–	–	–	–	1.73	3	3.19	8.29
28 GHz [67]	4-46	(30°/30°)	1.70	2.90	3.30	10.80	4.4	12.10	1.2	1.80	2.7	9.70
73 GHz [68]	4-46	(15°/15°)	1.63	3.06	3.30	8.76	5.51	8.94	1.36	2.30	2.81	8.71
142 GHz [68]	4-39	(8°/8°)	2.05	2.89	3.21	6.03	4.60	13.80	1.74	3.62	2.83	6.07

remarkable accuracy while being insensitive to measurement environment [28], as demonstrated in [54, Appendix A].

$$PL^{CI}(f_c, d_{3D}) \text{ [dB]} = \text{FSPL}(f_c, 1m)$$
$$+ 10n \log_{10}\left(\frac{d_{3D}}{d_0}\right) + \chi_\sigma,$$
$$\text{FSPL}(f_c, 1m) = 32.4 + 20 \log_{10}\left(\frac{f_c}{1 \text{ GHz}}\right), \quad (3)$$

where $\text{FSPL}(f_c, 1\text{ m})$ is obtained for carrier frequency f_c GHz at 1 m, n is the PLE, and χ_σ is large-scale shadow fading (zero-mean Gaussian r.v. with s.d. σ^{CI} in dB) [65].

The CI path loss model is extended for measurements conducted with V-H cross-polarized antennas by adding the constant attenuation parameter of the XPD. The model is known as the close-in reference distance with XPD (CIX) path loss model and uses the same PLE obtained from the CI path loss model for co-polarized V-V antenna measurements measured at identical locations. The XPD is evaluated by finding the minimum mean square error to best fit the measured cross-polarized path loss data with the PLE obtained from CI path loss modeling [52], and is derived in [54, Appendix A].

A. DIRECTIONAL PL MODELING
The evaluation of directional PL is based on the definitions for LOS, NLOS$_{\text{Best}}$, NLOS presented in [65, Table IV], where NLOS$_{\text{Best}}$ refers to the NLOS pointing direction with strongest received power in NLOS locations. Further, the NLOS definition encompasses non-boresight pointing directions in an azimuth sweep for T-R links with a clear visual boresight path. The scatter plot of the recorded PL in V-V configuration and the CI PL models are presented in Figure 10, with antenna gains removed. Scatter plots for the PL recorded in V-H configuration and the XPD evaluated from CIX PL models, with antenna gains removed, are presented in Figure 11.
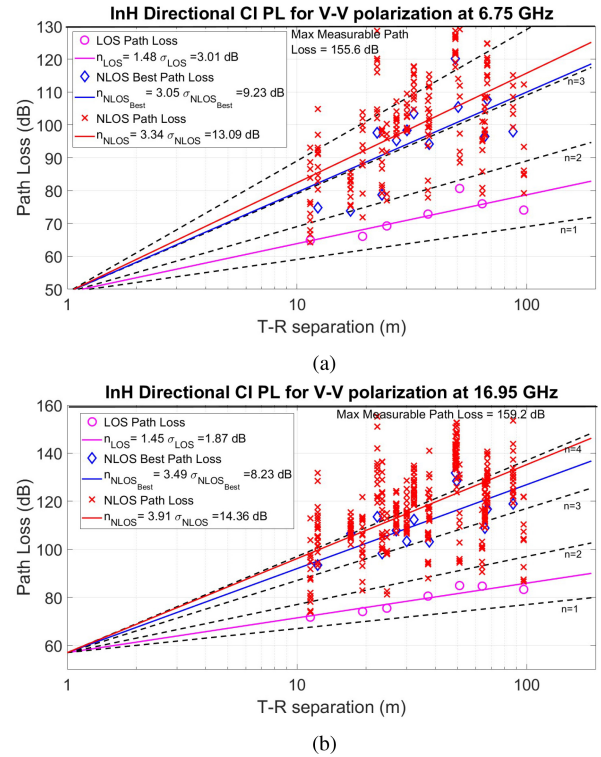

FIGURE 10. InH directional CI PL models and scatter plot for V-V polarization, removing antenna gains, at: (a) 6.75 GHz FR1(C); (b) 16.95 GHz FR3. [T-R separation: 11–97 m].

B. OMNIDIRECTIONAL PL MODELING
The omnidirectional received power is obtained by summing the directional received powers at each unique non-overlapping azimuth and elevation pointing angles removing the antenna gain, following the method taught in [61]. The scatter plots for CI and CIX modeling for the omnidirectional PL evaluated for V-V and V-H antenna configurations are presented in Figure 12 and 13, respectively.
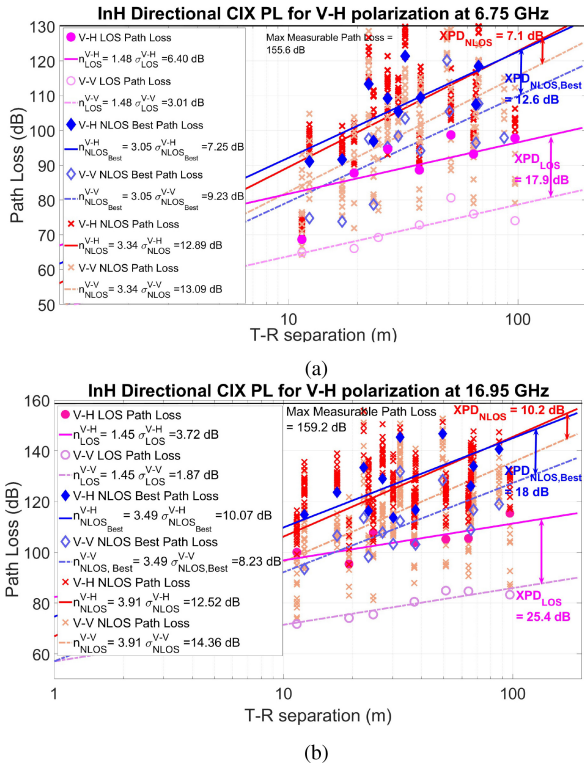
FIGURE 11. InH directional CIX PL models, scatter plot, and XPD for V-H polarization, removing antenna gains, at: (a) 6.75 GHz FR1(C); (b) 16.95 GHz FR3. [T-R separation: 11–97 m].

FIGURE 12. InH omnidirectional CI PL models and scatter plot for V-V polarization, removing antenna gains, at: (a) 6.75 GHz FR1(C); (b) 16.95 GHz FR3. [T-R separation: 11–97 m].

The CI PL model results for directional and omnidirectional PL, removing the antenna gains, are tabulated in Table 6 along with results from past measurement campaigns in indoor offices at mmWave (FR2) frequencies.

The LOS PLE is obtained as 1.48 at 6.75 GHz and 1.45 at 16.95 GHz, which are slightly lower (i.e., the channel is less lossy) than the directional LOS PLEs at 28, 73, and 142 GHz (1.7, 1.63, and 2.05, respectively). Further, the NLOS directional PLE at 6.75 and 16.95 GHz are 3.34 and 3.91, which are significantly lower than the PLEs at 28, 73, and 142 GHz (4.4, 5.51, and 4.6, respectively). The NLOS$_{\text{Best}}$ PLEs are found to be 3.05 and 3.49 at 6.75 and 16.95 GHz, respectively, which are comparable to higher mmWave channels. The CIX modeling for the directional PL yielded XPDs of 17.9 dB, 12.6 dB and 7.1 dB for LOS, NLOS$_{\text{Best}}$, and NLOS, respectively at 6.75 GHz. Likewise, at 16.95 GHz, the XPDs obtained are 25.4 dB, 18 dB, and 10.2 dB in LOS, NLOS$_{\text{Best}}$, and NLOS, respectively.

The omnidirectional PL modeling resulted in LOS PLEs of 1.34 at 6.75 GHz and 1.32 at 16.95 GHz. Similarly, NLOS PLEs of 2.72 and 3.05 are obtained at 6.75 GHz and 16.95 GHz, respectively, which are similar to the PLE values at the mmWave frequencies. As shown in Table 6, the 3GPP implementation of the CI model assigns a constant PLE across frequencies in both LOS and NLOS [69]. The omnidirectional XPDs from CIX modeling at 6.75 GHz are obtained as 14 dB and 11.14 dB in LOS
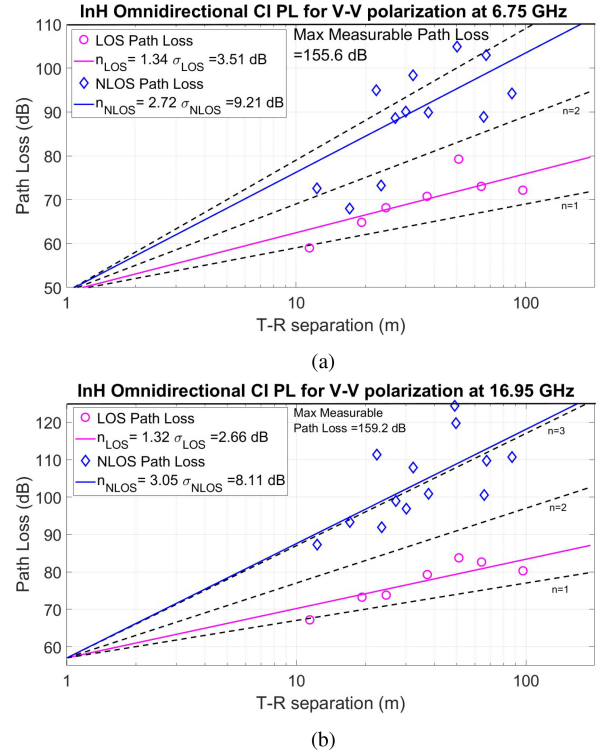
and NLOS, respectively. Similar modeling at 16.95 GHz resulted in XPDs of 22.1 dB in LOS and 19.6 dB in NLOS.

VI. SPATIO-TEMPORAL INH STATISTICS
A. RMS DELAY AND ANGULAR SPREAD
The RMS DS is a measure of the temporal dispersion of multipath in a wideband channel. The power threshold of 25 dB below PDP maxima or 5 dB above noise floor, discussed in Section II-A, is used to calculate RMS DS. The mean of the RMS DS observed in the directional PDPs captured in the 6.75 GHz campaign is obtained as 20.6 ns and 28.7 ns in LOS and NLOS, whereas, the directional RMS DS from the 16.95 GHz measurements are obtained as 19.5 ns and 14.9 ns. After synthesizing the omnidirectional PDP for each TX-RX location [61], the RMS DS in the omnidirectional PDP is observed as 37.7 ns and 48 ns in LOS and NLOS at 6.75 GHz, and 22.1 ns and 40.7 ns in LOS and NLOS at 16.95 GHz. It is clear that the 6.75 GHz band has slightly greater RMS DS compared to the 16.95 GHz band.

Further, Table 7 compares the RMS DS with measurement results at higher frequencies and for identical frequencies from the 3GPP model [66]. The RMS DS experiences a clear decreasing trend with increasing frequency, which is evident across both directional and omnidirectional RMS DS values in LOS and NLOS conditions. The RMS DS observations agree with the decreasing trend with increasing frequency modeled in 3GPP. At 6.75 GHz, the 3GPP model yields omnidirectional RMS DS values for LOS and NLOS as 19.9
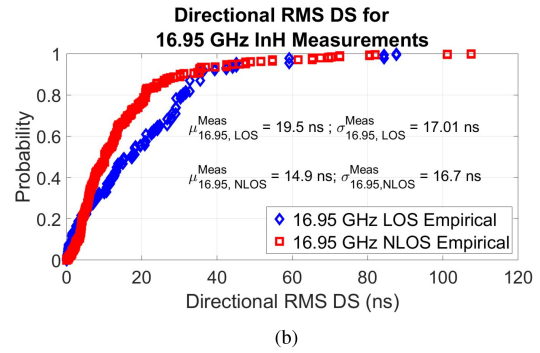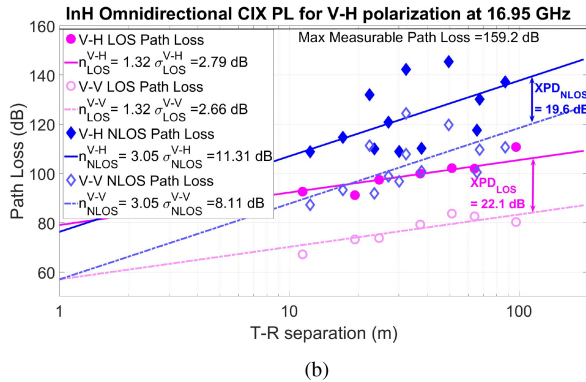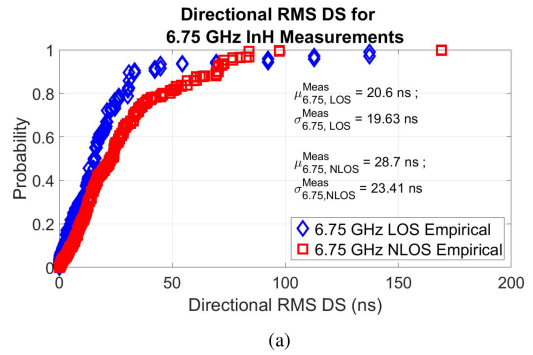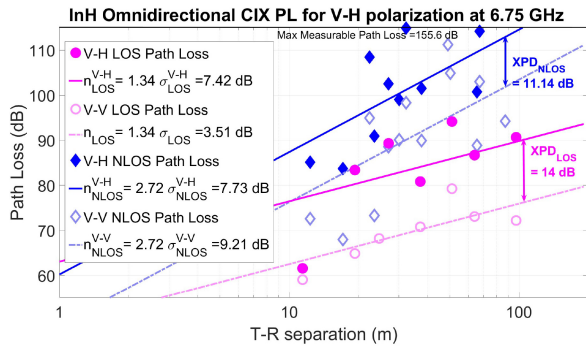
(a)

(b)

FIGURE 13. InH omnidirectional CIX PL models, scatter plot, and XPD for V-H polarization, removing antenna gains, at: (a) 6.75 GHz FR1(C); (b) 16.95 GHz FR3. [T-R separation: 11–97 m].

ns and 37.8 ns, respectively. Similarly, at 16.95 GHz (3GPP), the RMS DS values are 19.75 ns and 29.9 ns for LOS and NLOS, closely matching our data.

The RMS AS captures the azimuthal angular dispersion in the PAS, as shown in Figure 8. Figure 15 shows the CDF of the lobe and omni AS for the AOA PAS at 6.75 and 16.95 GHz for both LOS and NLOS scenarios. Mean RMS AS at 6.75 GHz and 16.95 GHz are tabulated in Table 7. The mean AS is found to be higher in NLOS than LOS for both lobe and omni AS, which has also been reported at higher frequencies [67], [68]. Omni AOA AS (ASA) are observed at 41° in LOS and 58° in NLOS at 6.75 GHz, whereas they are found lower at 16.95 GHz at 34° in LOS and 43° in NLOS. Comparing the measured RMS AS values with the 3GPP model, at 6.75 GHz (3GPP), the omnidirectional ASA values for LOS and NLOS are 40.9° and 58.2°, respectively. At 16.95 GHz (3GPP), the values are 34.89° and 53.09° for LOS and NLOS, respectively. 3GPP also models a decreasing trend of RMS AS with increasing frequency. This further confirms less multipath dispersion in both time and space at higher mmWave frequencies, as seen in [67], [68].

B. NUMBER OF TIME CLUSTERS AND MPCS PER CLUSTER

The numbers of time clusters and MPCs per cluster are determined based on the minimum inter-cluster time void interval (MTI). The MTI is the minimum time interval

(a)

(b)

(c)

(d)
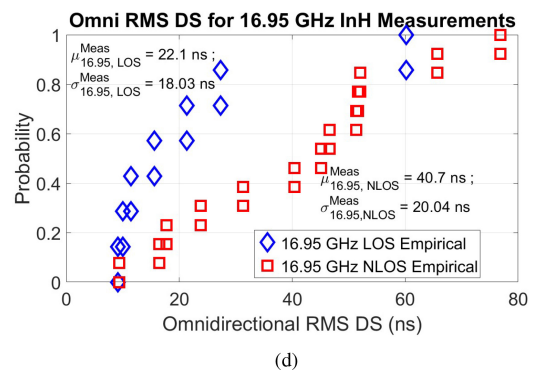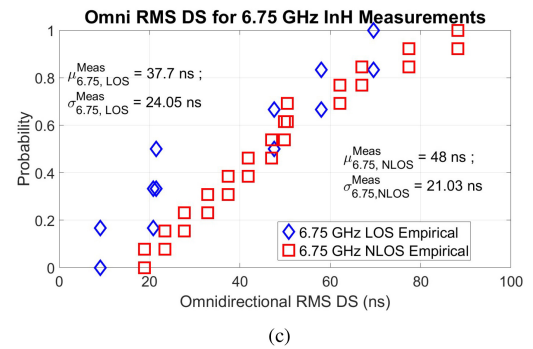
FIGURE 14. InH LOS and NLOS RMS DSs calculated at different frequencies and conditions: (a) Directional at 6.75 GHz; (b) Directional at 16.95 GHz; (c) Omni at 6.75 GHz; (d) Omni at 16.95 GHz.

between two separate time clusters. A larger MTI results in fewer time clusters with more MPCs per cluster [67], [68]. An MTI of 6 ns (determined by the corridor width at NYU WIRELESS, 2 m) is used for processing in this paper [57], [67]. The directional TCs are determined from

TABLE 7. RMS DS and AS characteristics from 6 GHz to 142 GHz for LOS and NLOS conditions in indoor environments and comparison to 3GPP models [66].

Frequency (GHz)	6.75 (This Work)	6.75 (3GPP)	16.95 (This Work)	16.95 (3GPP)	28 [67]	73 [68]	142 [68]
Dir RMS DS							
LOS [μ (ns)]	20.6	–	19.5	–	3.9	3.5	2.7
NLOS [μ (ns)]	28.7	–	14.9	–	14.5	10.0	7.2
Omni RMS DS							
LOS [μ (ns)]	37.7	19.9	22.1	19.75	10.8	6.2	3.0
NLOS [μ (ns)]	48	37.8	40.7	29.9	17.1	12.3	9.2
Lobe RMS ASA							
LOS [μ (°)]	9.4	–	5.4	–	Med:17.6	Med: 3.6	Med:3.4
NLOS [μ (°)]	24.5	–	14.3	–	Med:19.2	Med: 10.9	Med:4.4
Omni RMS ASA							
LOS [μ (°)]	40.9	40.93	34.2	34.89	Med:39.1	Med:23.3	Med:11.6
NLOS [μ (°)]	58.2	58.23	43.5	53.09	Med:31.8	Med:25.8	Med:5.4
Dir NumClusters							
LOS [μ]	3.8	–	3.8	–	1.4	1.3	1.2
NLOS$_{Best}$ [μ]	2.5	–	2	–	1.6	1.5	1.2
NLOS [μ]	3.4	–	2.7	–	3.4	2.6	2.4
Dir NumMPCperClusters							
LOS [μ]	5.4	–	4.3	–	2.4	2.5	2.1
NLOS$_{Best}$ [μ]	9	–	7.3	–	2.6	2.4	2.0
NLOS [μ]	6	–	4	–	3.2	2.8	1.2
Omni NumClusters							
LOS [μ]	4.1	15	4.4	15	4.6	2.8	1.9
NLOS [μ]	3.8	19	3.3	19	5.4	3.2	2.8
Omni NumMPCperClusters							
LOS [μ]	7.3	20	5.7	20	4.7	3.4	2.4
NLOS [μ]	13.7	20	13.2	20	6.4	3.2	2.2

directional PDPs generated following definitions highlighted in Section V-A. The resulting statistical mean of the numbers of time clusters (TC) and MPCs per cluster are tabulated in Table 7. Observing the mean values for number of TCs and MPCs in TCs, a clear decrease in total MPCs at higher frequencies indicating a sparser channel. The behavior is completely different from the constant numbers of TCs and MPCs in TCs used in the 3GPP modeling suggesting revisions for models for both TC and MPCs in each TC.

The adoption of high-gain directional antennas for the implementation of mmWave and sub-THz frequencies has seen enhancements in beamforming and beam-searching algorithms [70], [71], [72]. However, the sparsity of multipaths in the channel, as indicated in Table 7 at higher frequencies and susceptibility to blockage has proved a challenge for cellular services deployments. The FR1(C) and FR3 frequencies show richer multipath channels with greater temporal and spatial diversity, as shown in Table. 7. Using directional antenna arrays, the results show promise for greater throughput with multi-beam antenna combining for link improvement and spatial multiplexing implemented over higher rank channel matrices [44]. Past simulations at 142 GHz using NYUSIM have found limited gain from

spatial multiplexing due to channel sparsity [73]. Further, a strong isolation between the V and H polarizations, observed from Figures 11 and 13 allow for an additional degree of freedom in multiplexing.

VII. PENETRATION LOSS MEASUREMENT RESULTS
The penetration loss measurement results are presented in Table 8 and also in Table 10 in the Annex. For both co-polarized and cross-polarized antennas, the measured penetration loss exhibits minimal variation across the employed T-R separation distances. The co-pol penetration loss is calculated by linearly averaging L evaluated for V-V and H-H, while cross-pol penetration loss is obtained via the linear average of L for V-H and H-V, as detailed in Section IV-D. The penetration loss at 6.75 GHz is consistently lower compared to 16.75 GHz for both co and cross-polarized configurations. The largest loss measured is for the steel door exhibiting over 40 dB and 50 dB penetration loss at the 6.75 GHz and 16.95 GHz frequencies, respectively. The low-e glass curtain wall, used on the building outer surface, also exhibits strong attenuation of over 30 dB at both measurement frequencies for co and cross polarizations.
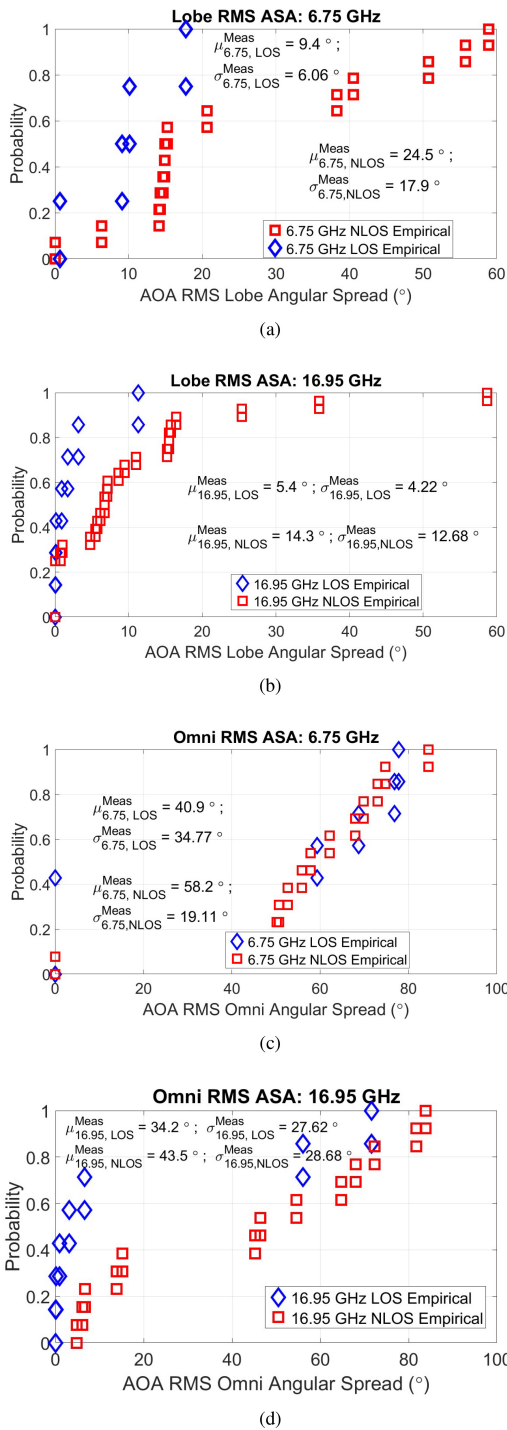
FIGURE 15. InH LOS and NLOS RMS AS for AOA PASs at different frequencies: (a) Lobe ASA at 6.75 GHz; (b) Lobe ASA at 16.95 GHz; (c) Omni ASA at 6.75 GHz; (d) Omni ASA at 16.95 GHz.

TABLE 8. Measured penetration loss of materials for Co-Pol and Cross-Pol for FR1(C) and FR3.

MUT	Width (cm)	Pol	Frequency				Δ_μ (dB)
			6.75 GHz		16.95 GHz		16.95−6.75 GHz
			μ (dB)	σ (dB)	μ (dB)	σ (dB)	
Cinderblock Wall	22	Co	13.4	1.6	15.0	1.1	1.6
		Cross	10.7	1.6	11.5	0.7	0.9
Low-e tinted glass wall	3	Co	33.7	0.9	42.3	0.2	8.6
		Cross	38.4	1.2	46.5	1.0	8.2
Low-e glass window	2	Co	29.7	1.4	32.7	2.6	3.0
		Cross	15.4	0.7	18.5	2.3	3.1
Clear Glass	1	Co	3.6	0.3	3.7	0.4	0.1
		Cross	4.2	0.4	4.4	0.6	0.2
Birch Wood panel	2	Co	2.4	0.7	6.1	0.4	3.7
		Cross	2.0	0.9	5.5	0.9	3.5
Wooden door	4.5	Co	5.8	1.1	6.1	1.3	0.3
		Cross	7.1	2.2	7.7	0.8	0.6
Steel door	4.7	Co	43.2	0.5	58.5	1.4	15.3
		Cross	41.8	0.8	56.4	1.7	14.6
Plasterboard wall	13.7	Co	2.1	1.0	4.5	0.4	2.4
		Cross	3.0	0.6	6.1	1.2	3.2
Drywall panel	3	Co	0.6	0.1	1.2	0.5	0.6
		Cross	1.5	0.2	2.3	1.2	0.8
White Board	3	Co	3.1	0.3	6.9	0.5	3.8
		Cross	4.1	0.7	7.5	1.3	3.4

strong dependence on polarization for low-e window glass attenuation.

Figure 16 (a) depicts the penetration loss of ten materials investigated in this paper at specific FR1(C) and FR3 frequencies, along with their penetration loss values in sub-6 GHz, mmWave, and sub-THz bands, as reported in [10], [20], [22], [23], [24], [74], [75], [76], [77], [78], [79]. To facilitate direct comparison of the material penetration loss across the entire frequency range of 0.5-150 GHz, the dB/cm penetration loss values for each material is multiplied by their respective thicknesses. The comparisons reveal an increasing penetration loss with increasing frequency for all ten of the materials measured. For example, the yellow rings for drywall in Figure 16(a) shows a clear increase with frequency when measurements from this paper are augmented with values reported in [74], [76], [78]. On the other hand, Figure 16 (b) only shows the penetration loss from the measurements conducted in this paper at 6.75 and 16.95 GHz.

A. COMPARISON WITH 3GPP MATERIAL PENETRATION LOSS MODEL

Penetration loss data in the 7–24 GHz range is sparse in the literature. Recent 3GPP discussions emphasize a critical gap in channel measurement and O2I loss data for the 7–24 GHz band. Over 80% of the channel measurement data submitted

The low-e window also shows significant attenuation, interestingly, loss for the cross-polarized configuration is much lower compared to the co-polarized measurements (29.7 dB Co Pol; 15.3 dB Cross Pol @ 6.75 GHz, and 32.68 dB Co Pol; 19.52 dB Cross Pol @ 16.95 GHz). This indicates a
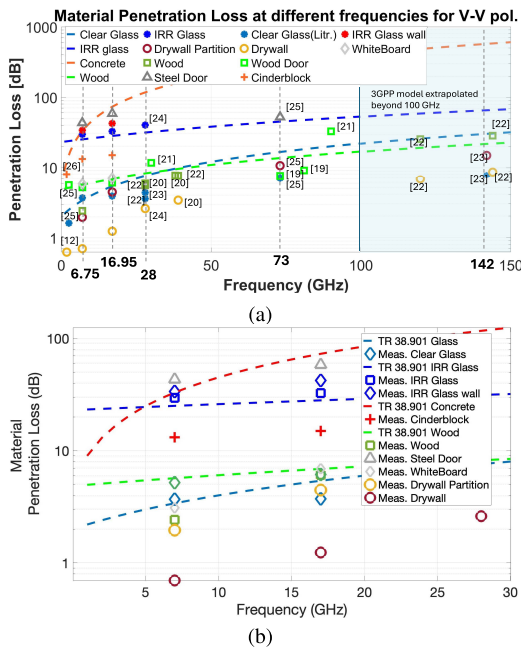
FIGURE 16. Penetration loss of various materials at different frequencies compared with the 3GPP TR-38.901 material penetration models. (a) Range 0-150 GHz. (b) Range 0-30 GHz.

TABLE 9. Comparison of measured penetration loss materials and TR 38.901 materials.

Measured Penetration Loss Material	TR 38.901 Material
Clear Glass	Standard multi-Pane Glass
Low-e Tinted Glass (Wall & Window)	IRR Glass
Cinderblock Wall	Concrete
Birch Wood Panel & Wooden Door	Wood

VIII. CONCLUSION

The world's first comprehensive indoor propagation measurement campaign for the FR1(C) and FR3 frequency bands at 6.75 GHz and 16.95 GHz, conducted in the indoor office/labs at the NYU WIRELESS Research Center was presented in this paper. The enhanced NYU channel sounder with absolute-timing measurement capability and co-located RF modules at 6.75 GHz and 16.95 GHz was highlighted. Moreover, the calibration and measurement procedures for location and material penetration loss measurements were detailed. The omnidirectional and directional CI PL modeling with a 1 m free space reference distance showed a familiar waveguiding effect in the indoor hallways with omni PLEs of 1.34 and 1.32 in LOS at 6.75 and 16.95 GHz, respectively. A decreasing trend in RMS DS with increasing frequency was observed when compared to mmWave FR2 frequencies, indicating multipath rich propagation at the FR3 and FR1(C) frequencies. Typical PASs showed widespread multipath arrival and departure directions at both frequencies. The RMS AS was found narrower at 16.95 GHz compared to 6.75 GHz.

Furthermore, the penetration loss exhibited by common materials found indoors and on building perimeters was reported in the paper. Penetration loss was consistently observed to be lower at 6.75 GHz compared to 16.75 GHz for co and cross-polarized antennas encompassing V-V, V-H, H-V, and H-H configurations. Low-e glass windows exhibited polarization-dependent attenuation of the signal. Upon comparing with penetration loss measurements at mmWave and sub-THz frequencies, the materials exhibited increasing loss at higher frequencies. Comparisons with the 3GPP models for material penetration show close adherence for wood and clear glass, while IRR glass and concrete showed RMSE errors above 10 dB, suggesting revisions may be required to current models. Reported material characteristics provide valuable information for future 5G and 6G wireless systems in the FR1(C) and FR3 upper mid-band spectrum. The empirical data and models showcased here will provide insights for future indoor propagation modeling in the frequency bands, supporting the analysis and design of future 5G and 6G wireless systems and networks in the upper mid-band spectrum.

IX. ANNEX: REPORTED MATERIAL PENETRATION LOSS
A. MATERIAL PENETRATION LOSS IN FR1(C) AND FR3
See Table 10.

in 3GPP falls outside the 7–24 GHz band, concentrated below 6 GHz or exceeding 28 GHz [80]. Thus, validation of the 3GPP TR 38.901 model for material penetration loss within the 7–24 GHz range is needed.

The current 3GPP model for material penetration loss (Table 7.4.3-1, 3GPP TR 38.901 Release 18 [66]) provides model parameters for concrete walls, IRR glass, standard multipane glass (clear glass), and wood that vary linearly with frequency. To compute the Root Mean Square Error (RMSE), the measured penetration loss materials are compared with materials in TR 38.901 as shown in Table 9. The RMSE calculated between the measured and the 3GPP predicted penetration losses for the materials at 6.75 GHz and 16.95 GHz, demonstrates a close adherence to the 3GPP model for conventional materials like clear glass (RMSE = 1.2 dB) and wood (RMSE = 2.4 dB). This indicates the 3GPP model validity for wood and standard multi-pane glass. Conversely, concrete walls and IRR glass walls exhibit significantly higher RMSE values (42.9 dB and 11.8 dB, respectively) at both frequencies. The 3GPP model consistently under-predicts the loss for IRR glass. However, for concrete walls, the observed discrepancy may be attributed to measurements in this paper characterizing penetration through an indoor cinderblock wall, which differs substantially from the thicker building exterior walls considered by the 3GPP model. Results suggest further investigation may be required for 3GPP material penetration models for IRR glass and concrete [69].

TABLE 10. Survey of penetration loss of materials in FR1(C) and FR3 bands from 4–24 GHz.

Frequency	MUT	Width [cm]	Penetration Loss [dB]	Pol.	Ref
4 GHz	Thick Heavily Reinforced Uniform Concrete Wall	35	20	co-pol	[20]
	Thick Slightly reinforced uniform concrete wall	12	15	co-pol	[20]
	Thick uniform plasterboard wall	12	10	co-pol	[20]
	Thick Slightly reinforced nonuniform concrete wall	12	8	co-pol	[20]
	Two layer glass	1.2	2.1	co-pol	[24]
	Single layer glass	0.85	1.8	co-pol	[24]
	Composite wooden door	7	6.5	co-pol	[24]
	2-layered energy efficient window with metal frame	N/A	26	co-pol	[26]
	Multi-layer wall of reinforced concrete and brick	45	28	co-pol	[26]
	3-layered energy efficient glass door with metal frame	N/A	32	co-pol	[26]
	2-layered energy efficient window with wooden frame	N/A	26	co-pol	[26]
	1-layered thin glass window with wooden frame	N/A	1.5	co-pol	[26]
5.85 GHz	Brick house exterior	N/A	14.5	co-pol	[16]
	Wood siding house exterior	N/A	8.8	co-pol	[16]
	Cinderblock wall	N/A	22	co-pol	[16]
	Plasterboard wall	N/A	4.7	co-pol	[16]
6.75 GHz	Cinderblock wall	22	13.4	co-pol	This Work, [25]
	Low-e tinted glass wall	3	33.7	co-pol	
	Low-e glass window	2	29.7	co-pol	
	Clear glass	1	3.6	co-pol	
	Birch wood panel	2	2.4	co-pol	
	Wooden door	4.5	5.8	co-pol	
	Steel door	4.7	43.2	co-pol	
	Plasterboard wall	13.7	2.1	co-pol	
	Drywall panel	3	0.6	co-pol	
	White Board	3	3.1	co-pol	
7 GHz	Thick Heavily Reinforced Uniform Concrete Wall	35	40	co-pol	[20]
	Thick Slightly reinforced uniform concrete wall	12	17.5	co-pol	[20]
	Thick uniform plasterboard wall	12	6	co-pol	[20]
	Thick Slightly reinforced nonuniform concrete wall	12	16	co-pol	[20]
	Two layer glass	1.2	2.6	co-pol	[24]
	Single layer glass	0.85	2.1	co-pol	[24]
	Composite wooden door	7	6.1	co-pol	[24]
	Wooden board 1	0.6	1.9	co-pol	[19]
	Wooden board 2	1.0	1.7	co-pol	[19]
	Wooden board 3	1.4	3.2	co-pol	[19]
	2-layered energy efficient window with metal frame	N/A	23	co-pol	[26]
	Multi-layer wall of reinforced concrete and brick	45	41	co-pol	[26]
	3-layered energy efficient glass door with metal frame	N/A	32	co-pol	[26]
	2-layered energy efficient window with wooden frame	N/A	30	co-pol	[26]
	1-layered thin glass window with wooden frame	N/A	5	co-pol	[81]

(Continued)

TABLE 10. (Continued.) Survey of penetration loss of materials in FR1(C) and FR3 bands from 4–24 GHz.

8 GHz	Thick Slightly reinforced uniform concrete wall	12	22	co-pol	[20]
	Thick uniform plasterboard wall	12	10	co-pol	[20]
	Thick Slightly reinforced nonuniform concrete wall	12	19	co-pol	[20]
	Two layer glass	1.2	2.7	co-pol	[24]
	Single layer glass	0.85	2.2	co-pol	[24]
	Composite wooden door	7	6.2	co-pol	[24]
	Wooden board 1	0.6	2	co-pol	[19]
	Wooden board 2	1	1.4	co-pol	[19]
	Wooden board 3	1.4	2.8	co-pol	[19]
	2-layered energy efficient window with metal frame	N/A	20	co-pol	[81]
	Multi-layer wall of reinforced concrete and brick	45	40	co-pol	[81]
	3-layered energy efficient glass door with metal frame	N/A	35	co-pol	[81]
	2-layered energy efficient window with wooden frame	N/A	27	co-pol	[81]
	1-layered thin glass window with wooden frame	N/A	8	co-pol	[81]
9 GHz	Thick Slightly reinforced uniform concrete wall	12	27	co-pol	[20]
	Thick uniform plasterboard wall	12	11	co-pol	[20]
	Thick Slightly reinforced nonuniform concrete wall	12	26	co-pol	[20]
	Two layer glass	1.2	2.8	co-pol	[24]
	Single layer glass	0.85	2.3	co-pol	[24]
	Composite wooden door	7	6.3	co-pol	[24]
	Wooden board 1	0.6	1.5	co-pol	[19]
	Wooden board 2	1	2	co-pol	[19]
	Wooden board 3	1.4	3	co-pol	[19]
	2-layered energy efficient window with metal frame	N/A	16	co-pol	[81]
	Multi-layer wall of reinforced concrete and brick	45	48	co-pol	[81]
	3-layered energy efficient glass door with metal frame	N/A	29	co-pol	[81]
	2-layered energy efficient window with wooden frame	N/A	30	co-pol	[81]
	1-layered thin glass window with wooden frame	N/A	8	co-pol	[81]
10 GHz	Thick Slightly reinforced uniform concrete wall	12	27	co-pol	[20]
	Thick uniform plasterboard wall	12	15	co-pol	[20]
	Thick Slightly reinforced nonuniform concrete wall	12	24	co-pol	[20]
	Two layer glass	1.2	2.9	co-pol	[24]
	Single layer glass	0.85	2.4	co-pol	[24]
	Composite wooden door	7	6.4	co-pol	[24]
	Wooden board 1	0.6	2.9	co-pol	[19]
	Wooden board 2	1	3	co-pol	[19]
	Wooden board 3	1.4	4.2	co-pol	[19]
	2-layered energy efficient window with metal frame	N/A	20	co-pol	[81]
	Multi-layer wall of reinforced concrete and brick	45	50	co-pol	[81]
	3-layered energy efficient glass door with metal frame	N/A	36	co-pol	[81]
	2-layered energy efficient window with wooden frame	N/A	29	co-pol	[81]
	1-layered thin glass window with wooden frame	N/A	8	co-pol	[81]
11 GHz	Thick Slightly reinforced uniform concrete wall	12	25	co-pol	[20]
	Thick uniform plasterboard wall	12	15	co-pol	[20]

(Continued)

TABLE 10. (Continued.) Survey of penetration loss of materials in FR1(C) and FR3 bands from 4–24 GHz.

11 GHz	Thick Slightly reinforced nonuniform concrete wall	12	24	co-pol	[20]
	Two layer glass	1.2	3	co-pol	[24]
	Single layer glass	0.85	2.5	co-pol	[24]
	Composite wooden door	7	6.5	co-pol	[24]
	Wooden board 1	0.6	2.6	co-pol	[19]
	Wooden board 2	1	1.8	co-pol	[19]
	Wooden board 3	1.4	4	co-pol	[19]
	2-layered energy efficient window with metal frame	N/A	29	co-pol	[26]
	Multi-layer wall of reinforced concrete and brick	45	49	co-pol	[26]
	3-layered energy efficient glass door with metal frame	N/A	32	co-pol	[26]
	2-layered energy efficient window with wooden frame	N/A	30	co-pol	[26]
	1-layered thin glass window with wooden frame	N/A	3	co-pol	[26]
12 GHz	Thick Slightly reinforced uniform concrete wall	12	27	co-pol	[20]
	Thick uniform plasterboard wall	12	16	co-pol	[20]
	Thick Slightly reinforced nonuniform concrete wall	12	26	co-pol	[20]
	Two layer glass	1.2	3	co-pol	[24]
	Single layer glass	0.85	2.6	co-pol	[24]
	Composite wooden door	7	6.6	co-pol	[24]
	Wooden board 1	0.6	1	co-pol	[19]
	Wooden board 2	1	1.9	co-pol	[19]
	Wooden board 3	1.4	3.9	co-pol	[19]
	2-layered energy efficient window with metal frame	N/A	28	co-pol	[26]
	Multi-layer wall of reinforced concrete and brick	45	50	co-pol	[26]
	3-layered energy efficient glass door with metal frame	N/A	28	co-pol	[26]
	2-layered energy efficient window with wooden frame	N/A	28	co-pol	[26]
	1-layered thin glass window with wooden frame	N/A	5	co-pol	[26]
13 GHz	Thick uniform plasterboard wall	12	16	co-pol	[20]
	Thick Slightly reinforced nonuniform concrete wall	12	26	co-pol	[20]
	Two layer glass	1.2	3.1	co-pol	[24]
	Single layer glass	0.85	2.7	co-pol	[24]
	Composite wooden door	7	6.7	co-pol	[24]
	Wooden board 1	0.6	2	co-pol	[19]
	Wooden board 2	1	4.4	co-pol	[19]
	Wooden board 3	1.4	4.8	co-pol	[19]
	2-layered energy efficient window with metal frame	N/A	26	co-pol	[26]
	Multi-layer wall of reinforced concrete and brick	45	60	co-pol	[26]
	3-layered energy efficient glass door with metal frame	N/A	29	co-pol	[26]
	2-layered energy efficient window with wooden frame	N/A	24	co-pol	[26]
	1-layered thin glass window with wooden frame	N/A	3	co-pol	[26]
14 GHz	Thick uniform plasterboard wall	12	17	co-pol	[20]
	Thick Slightly reinforced nonuniform concrete wall	12	27	co-pol	[20]
	Two layer glass	1.2	3.2	co-pol	[24]
	Single layer glass	0.85	2.8	co-pol	[24]
	Composite wooden door	7	6.8	co-pol	[24]
	Wooden board 1	0.6	3	co-pol	[19]

(Continued)

TABLE 10. (Continued.) Survey of penetration loss of materials in FR1(C) and FR3 bands from 4–24 GHz.

14 GHz	Wooden board 2	1	4.4	co-pol	[19]
	Wooden board 3	1.4	5.6	co-pol	[19]
	2-layered energy efficient window with metal frame	N/A	26	co-pol	[26]
	Multi-layer wall of reinforced concrete and brick	45	52	co-pol	[26]
	3-layered energy efficient glass door with metal frame	N/A	30	co-pol	[26]
	2-layered energy efficient window with wooden frame	N/A	31	co-pol	[26]
	1-layered thin glass window with wooden frame	N/A	10	co-pol	[26]
15 GHz	Thick Slightly reinforced uniform concrete wall	12	27	co-pol	[20]
	Thick uniform plasterboard wall	12	19	co-pol	[20]
	Thick Slightly reinforced nonuniform concrete wall	12	28	co-pol	[20]
	Two layer glass	1.2	3.3	co-pol	[24]
	Single layer glass	0.85	2.9	co-pol	[24]
	Composite wooden door	7	6.9	co-pol	[24]
	Wooden board 1	0.6	3	co-pol	[19]
	Wooden board 2	1	3.1	co-pol	[19]
	Wooden board 3	1.4	4.8	co-pol	[19]
	2-layered energy efficient window with metal frame	N/A	30	co-pol	[26]
	3-layered energy efficient glass door with metal frame	N/A	32	co-pol	[26]
	2-layered energy efficient window with wooden frame	N/A	34	co-pol	[26]
	1-layered thin glass window with wooden frame	N/A	6	co-pol	[26]
16 GHz	Thick uniform plasterboard wall	12	19	co-pol	[20]
	Thick Slightly reinforced nonuniform concrete wall	12	30	co-pol	[20]
	Two layer glass	1.2	3.4	co-pol	[24]
	Single layer glass	0.85	3	co-pol	[24]
	Composite wooden door	7	7	co-pol	[24]
	2-layered energy efficient window with metal frame	N/A	27	co-pol	[26]
	3-layered energy efficient glass door with metal frame	N/A	34	co-pol	[26]
	2-layered energy efficient window with wooden frame	N/A	40	co-pol	[26]
	1-layered thin glass window with wooden frame	N/A	4.5	co-pol	[26]
16.95 GHz	Cinderblock wall	22	15	co-pol	This Work, [25]
	Low-e tinted glass wall	3	42.3	co-pol	
	Low-e glass window	2	32.7	co-pol	
	Clear glass	1	3.7	co-pol	
	Birch wood panel	2	6.1	co-pol	
	Wooden door	4.5	6.1	co-pol	
	Steel door	4.7	58.5	co-pol	
	Plasterboard wall	13.7	4.5	co-pol	
	Drywall panel	3	1.2	co-pol	
	White Board	3	6.9	co-pol	
17 GHz	Thick uniform plasterboard wall	12	15	co-pol	[20]
	Thick Slightly reinforced nonuniform concrete wall	12	30	co-pol	[20]
	Two layer glass	1.2	3.5	co-pol	[24]
	Single layer glass	0.85	3.1	co-pol	[24]
	Composite wooden door	7	7.1	co-pol	[24]
	2-layered energy efficient window with metal frame	N/A	34	co-pol	[26]

(Continued)

TABLE 10. (Continued.) Survey of penetration loss of materials in FR1(C) and FR3 bands from 4–24 GHz.

17 GHz	3-layered energy efficient glass door with metal frame	N/A	35	co-pol	[26]
	2-layered energy efficient window with wooden frame	N/A	43	co-pol	[26]
	1-layered thin glass window with wooden frame	N/A	5	co-pol	[26]
18 GHz	Thick uniform plasterboard wall	12	11	co-pol	[20]
	Thick Slightly reinforced nonuniform concrete wall	12	32	co-pol	[20]
	Two layer glass	1.2	3.6	co-pol	[24]
	Single layer glass	0.85	3.2	co-pol	[24]
	Composite wooden door	7	7.2	co-pol	[24]
	2-layered energy efficient window with metal frame	N/A	33	co-pol	[26]
	1-layered thin glass window with wooden frame	N/A	7	co-pol	[26]
24 GHz	double pane glazed glass	2.4	5	co-pol	[81]

REFERENCES

[1] *NR; User Equipment (UE) Radio Transmission and Reception; Part 1: Range 1 Standalone, Version 18.5.0, Release 18*, 3GPP Standard TS 38.101, Mar. 2024.

[2] D.Shakya et al., "Propagation measurements and channel models in indoor environment at 6.75 GHz FR1(C) and 16.95 GHz FR3 upper-mid band spectrum for 5G and 6G," in *Proc. IEEE GLOBECOM*, 2024, pp. 1–6.

[3] "IEEE standard letter designations for radar-frequency bands," *IEEE Std 521-2019 (Revision of IEEE Std 521-2002)*, 2020.

[4] S. Kang et al., "Cellular wireless networks in the upper mid-band," *IEEE Open J. Commun. Soc.*, vol. 5, pp. 2058–2075, 2024.

[5] A. Davidson, *National Spectrum Strategy Implementation Plan*, Nat. Telecommun. Inf. Admin., Washington, DC, USA, Mar. 2024.

[6] (Nokia, Espoo, Finland). *Spectrum for 6G Explained*. (2024). Accessed: Apr. 2, 2024. [Online]. Available: https://www.nokia.com/about-us/newsroom/articles/spectrum-for-6g-explained/

[7] W. Tong and P. Zhu, *New Spectrum*. Cambridge, U.K.: Cambridge Univ. Press, 2021, pp. 146–157.

[8] *Study on the 7 to 24 GHz Frequency Range for NR*, 3GPP Standard TS 38.820, 2021. [Online]. Available: https://3gpp.org/DynaReport/38820.htm

[9] N. E. Klepeis et al., "The national human activity pattern survey (NHAPS): A resource for assessing exposure to environmental pollutants," *J. Expos. Sci. Environ. Epidemiol.*, vol. 11, no. 3, pp. 231–252, 2001.

[10] T. Rappaport and S. Sandhu, "Radio-wave propagation for emerging wireless personal-communication systems," *IEEE Antennas Propag. Mag.*, vol. 36, no. 5, pp. 14–24, Oct. 1994.

[11] R. Bultitude, "Measurement, characterization and modeling of indoor 800/900 MHz radio channels for digital communications," *IEEE Commun. Mag.*, vol. 25, no. 6, pp. 5–12, Jun. 1987.

[12] T. Rappaport and C. McGillem, "UHF fading in factories," *IEEE J. Sel. Areas Commun.*, vol. 7, no. 1, pp. 40–48, Jan. 1989.

[13] T. S. Rappaport et al., "Small-scale, local area, and transitional Millimeter wave propagation for 5G communications," *IEEE Trans. Antennas Propag.*, vol. 65, no. 12, pp. 6474–6490, Dec. 2017.

[14] G. R. MacCartney et al., "Millimeter-wave human blockage at 73 GHz with a simple double knife-edge diffraction model and extension for directional antennas," in *Proc. IEEE 84th Veh. Technol. Conf. (VTC)*, 2016, pp. 1–6.

[15] A. Bhardwaj et al., "Geometrical-empirical channel propagation model for human presence at 60 GHz," *IEEE Access*, vol. 9, pp. 38467–38478, 2021.

[16] G. Durgin, T. Rappaport, and H. Xu, "5.85-GHz radio path loss and penetration loss measurements in and around homes and trees," *IEEE Commun. Lett.*, vol. 2, no. 3, pp. 70–72, Mar. 1998.

[17] T. Schwengler and M. Glbert, "Propagation models at 5.8 GHz-path loss and building penetration," in *Proc. IEEE Radio Wireless Conf.*, 2000, pp. 119–124.

[18] A. Muqaibel et al., "Ultrawideband through-the-wall propagation," *IEEE Proc.-Microw., Antennas Propag.*, vol. 152, no. 6, pp. 581–588, Dec. 2005.

[19] "Discussion on channel model validation of TR38.901 for 7-24GHz," 3GPP, Gothenberg, Sweden, document 3GPP RAN1 Meeting #116, 3GPP R1-2403280, Apr. 2024.

[20] Y. Zhang and Y. Hwang, "Measurements of the characteristics of indoor penetration loss," in *Proc. IEEE Veh. Technol. Conf. (VTC)*, 1994, pp. 1741–1744.

[21] P. Ökvist et al., "15 GHz propagation properties assessed with 5G radio access prototype," in *Proc. IEEE 26th Annu. Int. Symp. Pers., Indoor, Mobile Radio Commun. (PIMRC)*, 2015, pp. 2220–2224.

[22] H. Zhao et al., "28 GHz millimeter wave cellular communication measurements for reflection and penetration loss in and around buildings in New York city," in *Proc. IEEE Int. Conf. Commun. (ICC)*, 2013, pp. 5163–5167.

[23] J. Ryan, G. R. MacCartney, and T. S. Rappaport, "Indoor office wideband penetration loss measurements at 73 GHz," in *Proc. IEEE Int. Conf. Commun. Workshops (ICC Workshops)*, 2017, pp. 228–233.

[24] Y. Du et al., "Measurement and modeling of penetration loss in the range from 2 GHz to 74 GHz," in *Proc. IEEE Globecom Workshops (GC Wkshps)*, 2016, pp. 1–6.

[25] D. Shakya et al., "Wideband penetration loss through building materials and partitions at 6.75 GHz in FR1(C) and 16.95 GHz in the FR3 upper mid-band spectrum," in *Proc. IEEE GLOBECOM 2024*, 2024, pp. 1–6.

[26] I. Rodriguez, H. C. Nguyen, N. T. K. Jorgensen, T. B. Sorensen, and P. Mogensen, "Radio propagation into modern buildings: Attenuation measurements in the range from 800 MHz to 18 GHz," in *Proc. IEEE 80th Veh. Technol. Conf. (VTC)*, 2014, pp. 1–5.

[27] X. Zhou et al., "Indoor wideband channel measurements and analysis at 11 and 14 GHz," *IET Microw., Antennas Propag.*, vol. 11, no. 10, pp. 1393–1400, 2017.

[28] S. Sun et al., "Investigation of prediction accuracy, sensitivity, and parameter stability of large-scale propagation path loss models for 5G wireless communications," *IEEE Trans. Veh. Technol.*, vol. 65, no. 5, pp. 2843–2860, May 2016.

[29] Q. Wei et al., "Measurement-based analysis of XL-MIMO channel characteristics in a corridor scenario," in *Proc. IEEE VTC*, 2024, pp. 1–6.

[30] N. O. Oyie and T. J. O. Afullo, "Measurements and analysis of large-scale path loss model at 14 and 22 GHz in indoor corridor," *IEEE Access*, vol. 6, pp. 17205–17214, 2018.

[31] G. J. Janssen, P. A. Stigter, and R. Prasad, "Wideband indoor channel measurements and BER analysis of frequency selective multipath channels at 2.4, 4.75, and 11.5 GHz," *IEEE Trans. Commun.*, vol. 44, no. 10, pp. 1272–1288, Oct. 1996.

[32] T. Rappaport and D. Hawbaker, "Wide-band microwave propagation parameters using circular and linear polarized antennas for indoor wireless channels," *IEEE Trans. Commun.*, vol. 40, no. 2, pp. 240–245, Feb. 1992.

[33] S. Y. Seidel and T. S. Rappaport, "914 MHz path loss prediction models for indoor wireless communications in multifloored buildings," *IEEE Trans. Antennas Propag.*, vol. 40, no. 2, pp. 207–217, Feb. 1992.

[34] S. Deng, G. R. MacCartney, and T. S. Rappaport, "Indoor and outdoor 5G diffraction measurements and models at 10, 20, and 26 GHz," in *Proc. IEEE Glob. Commun. Conf. (GLOBECOM)*, 2016, pp. 1–7.

[35] H. Miao et al., "Sub-6 GHz to mmWave for 5G-advanced and beyond: Channel measurements, characteristics and impact on system performance," *IEEE J. Sel. Areas Commun.*, vol. 41, no. 6, pp. 1945–1960, Jun. 2023.

[36] M. Kim, Y. Konishi, Y. Chang, and J.-I. Takada, "Large scale parameters and double-directional Characterization of indoor wideband radio multipath channels at 11 GHz," *IEEE Trans. Antennas Propag.*, vol. 62, no. 1, pp. 430–441, Jan. 2014.

[37] M. B. Majed et al., "Channel characterization and path loss modeling in indoor environment at 4.5, 28, and 38 GHz for 5G cellular networks," *Int. J. Antennas Propag.*, vol. 2018, no. 1, Sep. 2018, Art. no. 9142367.

[38] A. M. Al-Samman, T. Abd Rahman, and M. H. Azmi, "Indoor corridor wideband radio propagation measurements and channel models for 5G millimeter wave wireless communications at 19 GHz, 28 GHz, and 38 GHz bands," *Wireless Commun. Mobile Comput.*, vol. 2018, no. 1, 2018, Art. no. 6369517.

[39] Y. Wang, W. Lu, and H. Zhu, "An empirical path-loss model for wireless channels in indoor short-range office environment," *Int. J. Antennas Propag.*, vol. 2012, no. 1, 2012, Art. no. 636349.

[40] X. Yin, Y. Ji, and H. Yan, "Measurement-based Characterization of 15 GHz propagation channels in a laboratory environment," *IEEE Access*, vol. 5, pp. 1428–1438, 2017.

[41] I. Rodriguez et al., "An empirical outdoor-to-indoor path loss model from below 6 GHz to cm-Wave frequency bands," *IEEE Antennas Wireless Propag. Lett.*, vol. 16, pp. 1329–1332, 2017.

[42] C. A. L. Diakhate et al., "Millimeter-wave outdoor-to-indoor channel measurements at 3, 10, 17 and 60 GHz," in *Proc. 11th Eur. Conf. Antennas Propag. (EUCAP)*, 2017, pp. 1798–1802.

[43] O. Landron, M. Feuerstein, and T. Rappaport, "A comparison of theoretical and empirical reflection coefficients for typical exterior wall surfaces in a mobile radio environment," *IEEE Trans. Antennas Propag.*, vol. 44, no. 3, pp. 341–351, Mar. 1996.

[44] S. Sun et al., "Millimeter wave multi-beam antenna combining for 5G cellular link improvement in New York city," in *Proc. IEEE Int. Conf. Commun. (ICC)*, 2014, pp. 5468–5473.

[45] G. Naik et al., "Next generation Wi-Fi and 5G NR-U in the 6 GHz bands: Opportunities and challenges," *IEEE Access*, vol. 8, pp. 153027–153056, 2020.

[46] F. Liu et al., "Integrated sensing and communications: Toward dual-functional wireless networks for 6G and beyond," *IEEE J. Sel. Areas Commun.*, vol. 40, no. 6, pp. 1728–1767, Jun. 2022.

[47] D. Shakya, T. Wu, M. E. Knox, and T. S. Rappaport, "A wideband sliding correlation channel sounder in 65 nm CMOS: Evaluation board performance," *IEEE Trans. Circuits Syst. II, Exp. Briefs*, vol. 68, no. 9, pp. 3043–3047, Sep. 2021.

[48] G. R. MacCartney and T. S. Rappaport, "A flexible millimeter-wave channel sounder with absolute timing," *IEEE J. Sel. Areas Commun.*, vol. 35, no. 6, pp. 1402–1418, Jun. 2017.

[49] T. S. Rappaport, *Wireless Communications: Principles and Practice*. Cambridge, U.K.: Cambridge Univ. Press, 2024.

[50] T. Wu, T. S. Rappaport, and C. M. Collins, "Safe for generations to come: Considerations of safety for Millimeter waves in wireless communications," *IEEE Microw. Mag.*, vol. 16, no. 2, pp. 65–84, Mar. 2015.

[51] C. Cho et al., "Ionizing radiation exposure after allogeneic hematopoietic cell transplantation," *Bone Marrow Transplant.*, vol. 57, no. 5, pp. 827–829, 2022.

[52] S. Ju, D. Shakya, H. Poddar, Y. Xing, O. Kanhere, and T. S. Rappaport, "142 GHz sub-Terahertz radio propagation measurements and channel characterization in factory buildings," *IEEE Trans. Wireless Commun.*, vol. 23, no. 7, pp. 7127–7143, Jul. 2024.

[53] O. Kanhere and T. S. Rappaport, "Calibration of NYURay, a 3D mmWave and sub-THz ray tracer using indoor, outdoor, and factory channel measurements," in *Proc. IEEE ICC*, 2023, pp. 1–6.

[54] G. R. Maccartney, T. S. Rappaport, S. Sun, and S. Deng, "Indoor office wideband millimeter-wave propagation measurements and channel models at 28 and 73 GHz for ultra-dense 5G wireless networks," *IEEE Access*, vol. 3, pp. 2388–2424, 2015.

[55] D. Shakya, H. Poddar, and T. S. Rappaport, "A sub-Terahertz sliding Correlator channel sounder with absolute timing using precision time protocol over Wi-Fi," in *Proc. IEEE Glob. Commun. Conf.*, 2023, pp. 5793–5798.

[56] T. S. Rappaport, K. A. Remley, C. Gentile, A. F. Molisch, and A. Zajiĉ, Eds., *Radio Propagation Measurements and Channel Modeling: Best Practices for Millimeter-Wave and Sub-Terahertz Frequencies*. Cambridge, U.K.: Cambridge Univ. Press, 2022.

[57] D. Shakya, S. Ju, O. Kanhere, H. Poddar, Y. Xing, and T. S. Rappaport, "Radio propagation measurements and statistical channel models for outdoor urban microcells in open squares and streets at 142, 73, and 28 GHz," *IEEE Trans. Antennas Propag.*, vol. 72, no. 4, pp. 3580–3595, Apr. 2024.

[58] Y. Xing, O. Kanhere, S. Ju, T. S. Rappaport, and G. R. MacCartney, "Verification and calibration of antenna cross-Polarization discrimination and penetration loss for millimeter wave communications," in *Proc. IEEE 88th Veh. Technol. Conf. (VTC)*, 2018, pp. 1–6.

[59] W. G. Newhall and T. Rappaport, "An antenna pattern measurement technique using wideband channel profiles to resolve multipath signal components," in *Proc. 19th Annu. Meeting Symp. Antenna Meas. Techn. Assoc.*, 1997, pp. 1–6.

[60] W. G. Newhall, T. Rappaport, and D. G. Sweeney, "A spread spectrum sliding correlator system for propagation measurements," *RF Design*, pp. 40–54, Apr. 1996.

[61] S. Sun et al., "Synthesizing omnidirectional antenna patterns, received power and path loss from directional antennas for 5G millimeter-wave communications," in *Proc. IEEE GLOBECOM*, 2015, pp. 1–7.

[62] S. Ju and T. S. Rappaport, "Statistical channel model of Wideband sub-THz radio propagation in indoor factories at 142 GHz: Towards 6G industrial wireless networks," *IEEE Trans. Wireless Commun.*, to be published.

[63] Y. Xing, O. Kanhere, S. Ju, and T. S. Rappaport, "Indoor wireless channel properties at Millimeter wave and sub-terahertz frequencies," in *Proc. IEEE GLOBECOM*, 2019, pp. 1–6.

[64] D. Shakya, D. Chizhik, J. Du, R. A. Valenzuela, and T. S. Rappaport, "Dense urban outdoor-indoor coverage from 3.5 to 28 GHz," in *Proc. IEEE Int. Conf. Commun.*, 2022, pp. 932–937.

[65] T. S. Rappaport, G. R. MacCartney, M. K. Samimi, and S. Sun, "Wideband millimeter-wave propagation measurements and channel models for future wireless communication system design," *IEEE Trans. Commun.*, vol. 63, no. 9, pp. 3029–3056, Sep. 2015.

[66] "Study on channel model for frequencies from 0.5 to 100 GHz; (Release 16), Version V16.1.0," 3GPP, Sophia Antipolis, France, Rep. TR 38.901, Dec. 2019.

[67] S. Ju, Y. Xing, O. Kanhere, and T. S. Rappaport, "Millimeter wave and sub-terahertz spatial statistical channel model for an indoor office building," *IEEE J. Sel. Areas Commun.*, vol. 39, no. 6, pp. 1561–1575, Jun. 2021.

[68] Y. Xing, T. S. Rappaport, and A. Ghosh, "Millimeter wave and sub-THz indoor radio propagation channel measurements, models, and comparisons in an office environment," *IEEE Commun. Lett.*, vol. 25, no. 10, pp. 3151–3155, Oct. 2021.

[69] "Channel model validation of TR 38.901 for 7-24 GHz," 3GPP, Gothenberg, Sweden, document TSG RAN WG1 #116, 3GPP R1-2402407, Apr. 2024.

[70] B. Ning et al., "Beamforming technologies for ultra-massive MIMO in terahertz communications," *IEEE Open J. Commun. Soc.*, vol. 4, pp. 614–658, 2023.

[71] S. Sun, T. S. Rappaport, M. Shafi, and H. Tataria, "Analytical framework of hybrid beamforming in multi-cell millimeter-wave systems," *IEEE Trans. Wireless Commun.*, vol. 17, no. 11, pp. 7528–7543, Nov. 2018.

[72] T. S. Rappaport et al., "38 GHz and 60 GHz angle-dependent propagation for cellular & peer-to-peer wireless communications," in *Proc. IEEE Int. Conf. Commun. (ICC)*, 2012, pp. 4568–4573.

[73] S. Ju and T. S. Rappaport, "Sub-Terahertz spatial statistical MIMO channel model for urban microcells at 142 GHz," in *Proc. IEEE Glob. Commun. Conf. (GLOBECOM)*, 2021, pp. 1–6.

[74] M. Khatun, C. Guo, D. Matolak, and H. Mehrpouyan, "Indoor and outdoor penetration loss measurements at 73 and 81 GHz," in *Proc. IEEE Glob. Commun. Conf. (GLOBECOM)*, 2019, pp. 1–5.

[75] C. E. O. Vargas and L. D. S. Mello, "Measurements of reflection and penetration loss of construction materials at 28 GHz and 38 GHz," in *Proc. IEEE-APS Top. Conf. Antennas Propag. Wireless Commun. (APWC)*, 2018, pp. 897–900.

[76] D. W. Matolak, M. Mohsen, and J. Liu, "Building material attenuations at 5 GHz and at mmWave frequencies 30 GHz and 90 GHz," in *Proc. IEEE 21st Annu. Wireless Microw. Technol. Conf. (WAMICON)*, 2021, pp. 1–4.

[77] K. Du, O. Ozdemir, F. Erden, and I. Guvenc, "Sub-terahertz and mmWave penetration loss measurements for indoor environments," in *Proc. IEEE Int. Conf. Commun. Workshops (ICC Workshops)*, 2021, pp. 1–6.

[78] Y. Xing and T. S. Rappaport, "Propagation measurement system and approach at 140 GHz-moving to 6G and above 100 GHz," in *Proc. IEEE Glob. Commun. Conf. (GLOBECOM)*, 2018, pp. 1–6.

[79] S. Nie, G. R. MacCartney, S. Sun, and T. S. Rappaport, "72 GHz millimeter wave indoor measurements for wireless and backhaul communications," in *Proc. IEEE 24th PIMRC*, 2013, pp. 2429–2433.

[80] "Study on channel modelling enhancements for 7-24GHz for NR," 3GPP, Gothenberg, Sweden, document TSG RAN Meeting #102, 3GPP RP-234018, Dec. 2023.

[81] Y. C. Lee, S.-S. Oh, C. W. Byeon, K. Aziding, and B.-L. Cho, "Impact of window penetration loss on building entry loss from 3.5 to 24 GHz," *IEEE Access*, vol. 9, pp. 138571–138579, 2021.

THEODORE S. RAPPAPORT (Fellow, IEEE) received the Ph.D. degree from Purdue University in 1987.

He is the David Lee/Ernst Weber Professor with New York University (NYU) and holds faculty appointments with the Electrical and Computer Engineering Department, NYU Tandon School of Engineering, the Courant Computer Science Department, and the NYU Langone School of Medicine. He is the Founding Director of NYU WIRELESS, a multidisciplinary research center focused on the future of wireless communications and applications. His research has led the way for modern wireless communication systems. His Ph.D. degree provided fundamental knowledge of indoor wireless channels used to create the first Wi-Fi standard (IEEE 802.11), and he conducted fundamental work that led to the first U.S. digital cellphone standards, TDMA IS-54/IS-136, and CDMA IS-95. He pioneered the use of site-specific design and optimization of wireless networks, and he and his students engineered the world's first public Wi-Fi hotspots. His work proved the viability of millimeter waves for mobile communications, and the global wireless industry adopted his vision for 5th generation (5G) millimeter-wave cellphone networks. His most recent research has proven the viability of subterahertz wireless communications and position location for 6G, 7G, and beyond. He founded three academic wireless research centers at Virginia Tech, The University of Texas, and NYU that have produced thousands of engineers and educators since 1990, and he has co-authored over 300 papers and 20 books, including the most cited books on wireless communications, adaptive antennas, wireless simulation, and millimeter-wave communications. He co-founded two wireless companies, TSR Technologies and Wireless Valley Communication, which were sold to publicly traded companies, and he has advised many others. He co-founded the Virginia Tech Symposium on Wireless Communications in 1991, the Texas Wireless Summit in 2003, and the Brooklyn 5G Summit in 2014. He has more than 100 patents issued and pending.

Dr. Rappaport has received the IEEE's Eric Sumner Award, the ASEE's Terman Award, The Sir Monty Finniston Medal from the Institution of Engineering and Technology, the IEEE Vehicular Technology Society's James R. Evans Avant Garde and Stu Meyer Awards, the IEEE Education Society William E. Sayle Award for achievement in education, the IEEE Communications Society Armstrong Award, and the Armstrong Medal and Sarnoff Citation from the Radio Club of America. He served on the Technological Advisory Council of the Federal Communications Commission, is a member of the National Academy of Engineering and the Wireless Hall of Fame, is a Fellow of the Radio Club of America and the National Academy of Inventors, a Life Member of the American Radio Relay League, a licensed Professional Engineer in Texas and Virginia, and an Amateur Radio Operator (N9NB).

DIPANKAR SHAKYA (Member, IEEE) received the B.E. degree in electronics and communications from Tribhuvan University, Nepal, in 2016, and the M.S. degree in electrical engineering from New York University in 2021. He is currently pursuing the Ph.D. degree in electrical engineering with the NYU WIRELESS Research Center, New York University Tandon School of Engineering, Brooklyn, NY, USA, under the supervision of Prof. T. S. Rappaport. In 2019, he joined the NYU WIRELESS Research Center, following three years of service as an Engineer for flood early warning systems in South Asia. His research interests include mid-band, millimeter-wave, and terahertz channel propagation measurements, modeling, RF circuit design, and metrology.

MINGJUN YING (Graduate Student Member, IEEE) received the B.E. degree in communication engineering from the Chongqing University of Posts and Telecommunications, Chongqing, China, in 2023. He is currently pursuing the Ph.D. degree in electrical engineering with the NYU WIRELESS Research Center, New York University Tandon School of Engineering, Brooklyn, NY, USA, under the supervision of Prof. T. S. Rappaport. His research interests include green communication, channel modeling, adversarial communication, satellite communications, and integrated sensing and communication.

HITESH PODDAR (Member, IEEE) received the B.Tech. degree in electronics and communication engineering from VIT, Vellore, in 2017, the M.Tech. degree in embedded systems from BITS, Pilani, in 2022, and the M.S. degree in electrical engineering from the New York University (NYU) WIRELESS Research Center, NYU, USA, in 2023, under the supervision of Prof. T. S. Rappaport. He is currently a Senior Communication Systems Researcher with the Department of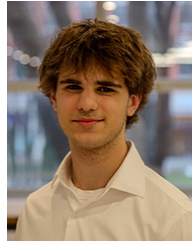 Systems, Algorithms, and Services, Sharp Laboratories of America, USA. Prior to pursuing his M.S. degree, he was a Physical Layer Software Developer with Qualcomm for four years, where he gained extensive experience in 2G (GSM + EDGE) and 5G-NR (beam management) technologies. His work primarily focused on algorithm design, implementation, debugging critical issues, testing, and maintenance for the physical layer. He worked on the bring-up, development, and optimization of 5G-NR beam management software for Qualcomm chipsets, which has become an essential component of 5G systems. His primary research interests include mmWave and sub-THz radio propagation measurement and channel modeling.

PEIJIE MA was graduated from Shanghai Jiao Tong University Affiliated Middle School Jiading Campus. He is currently pursuing the B.S. degree in computer engineering with New York University, Brooklyn, NY, USA. He was involved in the upper mid-band radio propagation research in Spring 2024 with Prof. Theodore S. Rappaport's Group, NYU WIRELESS Research Center. His current research interests focus on semiconductors, IC architecture design, and millimeter-wave propagation.

IDRIS AL-WAZANI received the high school education from Shanghai American School and graduated high school from Yongsan International School of Seoul in 2023. He is currently pursuing the B.S. degree in electrical engineering with New York University. He is currently involved in the radio propagation research conducted by Prof. Theodore S. Rappaport's Group, NYU WIRELESS Research Center at FR3 and FR1C frequencies. His research interests include electronics hardware, emerging media, channel propagation measurements, channel modeling, and beamforming approaches at upper mid-band, mmWave, and THz frequencies.

YANBO WANG is currently pursuing the B.S. degree in electrical and computer engineering with New York University Tandon School of Engineering. He was involved in the FR1C and FR3 propagation research with NYU WIRELESS under Prof. T. S. Rappaport in Spring 2024. His research interests include digital signal processing, image processing, computer vision, and human–robot interaction.